

The ICON (ICOsahedral Non-hydrostatic) modelling framework of DWD and MPI-M: Description of the non-hydrostatic dynamical core

Günther Zängl,* Daniel Reinert, Pilar Rípodas and Michael Baldauf

Deutscher Wetterdienst, Offenbach, Germany

*Correspondence to: G. Zängl, German Weather Service, Frankfurter Str. 135, 63067 Offenbach, Germany.
E-mail: Guenther.Zaengl@dwd.de

This article describes the non-hydrostatic dynamical core developed for the ICOsahedral Non-hydrostatic (ICON) modelling framework. ICON is a joint project of the German Weather Service (DWD) and the Max Planck Institute for Meteorology (MPI-M), targeting a unified modelling system for global numerical weather prediction (NWP) and climate modelling. Compared with the existing models at both institutions, the main achievements of ICON are exact local mass conservation, mass-consistent tracer transport, a flexible grid nesting capability and the use of non-hydrostatic equations on global domains. The dynamical core is formulated on an icosahedral-triangular Arakawa C grid. Achieving mass conservation is facilitated by a flux-form continuity equation with density as the prognostic variable. Time integration is performed with a two-time-level predictor–corrector scheme that is fully explicit, except for the terms describing vertical sound-wave propagation. To achieve competitive computational efficiency, time splitting is applied between the dynamical core on the one hand and tracer advection, physics parametrizations and horizontal diffusion on the other hand. A sequence of tests with varying complexity indicates that the ICON dynamical core combines high numerical stability over steep mountain slopes with good accuracy and reasonably low diffusivity. Preliminary NWP test suites initialized with interpolated analysis data reveal that the ICON modelling system already achieves better skill scores than its predecessor at DWD, the operational hydrostatic Global Model Europe (GME), and at the same time requires significantly fewer computational resources.

Key Words: model development; numerical weather prediction; dynamical cores

Received 24 October 2013; Revised 24 March 2014; Accepted 26 March 2014; Published online in Wiley Online Library 2 June 2014

1. Introduction

With the advancing progress of supercomputer performance, the spatial resolution affordable for cutting-edge research applications in global atmospheric modelling reached non-hydrostatic scales in the mid-2000s (Tomita and Satoh, 2004; Satoh *et al.*, 2008). By the end of this decade, operational numerical weather prediction (NWP) for the globe will also reach mesh sizes for which a non-hydrostatic dynamical core becomes necessary. Consequently, several research institutions and weather prediction centres around the world have developed or are developing non-hydrostatic global atmospheric models. As it is clear that future high-performance computing will rely on massively parallel algorithms working on $O(10^4 - 10^6)$ cores, there is a general trend away from spectral transform models and regular latitude–longitude grids, which impose limits on scalability because of their need for extensive global communication. While global spectral transform models involve Fourier and Legendre transforms every time step, grid-point models formulated on

a latitude–longitude grid usually need a polar filter in order to mitigate the time step/numerical stability restrictions that would otherwise be induced by the convergence of meridians. Additional disadvantages of spectral transform models include the lack of an obvious way to achieve local mass conservation and mass-consistent tracer transport, which are essential for climate modelling and at least desirable for NWP. The majority of the newly developed global non-hydrostatic models are based on icosahedral grids (Tomita and Satoh, 2004; Walko and Avissar, 2008), centroidal Voronoi grids (Skamarock *et al.*, 2012) or cubed-sphere grids (Ullrich and Jablonowski, 2012), but other options such as yin–yang grids (Quaddouri and Lee, 2011) are also being considered. At the same time, there is a trend towards unified modelling systems for global and regional applications in order to spend the available (staff) resources for model development more efficiently and to keep the ever-increasing technical complexity of the software infrastructure (e.g. I/O, parallelization, atmosphere–ocean coupling) manageable. Thus, most of the recent developments include some means of using

non-uniform resolution, for instance by grid stretching, mesh refinement or conventional one-way and two-way nesting, and related options of running the models on limited-area domains.

Here we describe the non-hydrostatic dynamical core developed for the ICOSahedral Non-hydrostatic (ICON) modelling framework, which is a joint project between the German Weather Service (DWD) and the Max Planck Institute for Meteorology (MPI-M) for developing a unified next-generation global NWP and climate modelling system. The main goals formulated in the initial phase of the collaboration were as follows:

- better conservation properties than in the existing global models GME (Majewski *et al.*, 2002) and ECHAM (Stevens *et al.*, 2013), with the obligatory requirements of exact local mass conservation and mass-consistent tracer transport and the additional wish to achieve energy conservation;
- better scalability on future massively parallel high-performance computing architectures; and
- the availability of some means of static mesh refinement, which was subsequently concretized into the capability of mixing one-way nested and two-way nested grids within one model application, combined with an option for vertical nesting in order to allow the global grid to extend into the mesosphere (which greatly facilitates the assimilation of satellite data), whereas the nested domains extend only into the lower stratosphere in order to save computing time.

Despite some conceptual disadvantages pointed out by Gassmann (2011), including the necessity to give up the goal of exact energy conservation and the need for numerical filtering because of an unphysical stationary mode in the gravity-wave dispersion relationship, the decision has been made to employ an icosahedral-triangular C grid rather than a hexagonal grid, because of the more obvious way of implementing a hierarchical nesting-based mesh refinement. This grid type has already been used by Walko and Avissar (2008), applying a pure finite-volume discretization and a shaved-cell representation of topography. The work presented here builds upon the hydrostatic dynamical core of the ICON modelling framework described by Wan *et al.* (2013) by using the same discretizations for the basic mathematical operators (e.g. gradient, divergence, vorticity) but applies a different time-stepping scheme and a set of measures to minimize the amount of computational diffusion needed to ensure numerical stability. As will be shown, the kinetic energy spectra now lie within the range typically found for models with quadrilateral or hexagonal C grids. Moreover, the grid imprinting and the phase-speed errors of marginally resolved Rossby waves showing up in the Jablonowski and Williamson (2006a) test could be significantly reduced compared with the hydrostatic version. Preliminary results for real-case test suites initialized with interpolated analysis data indicate a substantial improvement over the Global Model Europe (GME) run in a comparable set-up, indicating that a proper physics–dynamics coupling has already been achieved.

Section 2 of this article proceeds with a detailed description of the dynamical core, focusing on its discretization in space and time and complemented by some remarks on physics–dynamics coupling. The results of a hierarchy of validation tests will be presented in section 3, followed by a summary of our main achievements in section 4. The appendices provide details about some special aspects of discretizing the equations of motion on a triangular C grid, followed by a linear stability analysis of our space–time discretization. A description of the grid-nesting algorithm is reserved for a separate article.

2. The dynamical core and its numerical implementation

2.1. The icosahedral grid

ICON employs an unstructured triangular grid that is based on successive refinement of a spherical icosahedron, which consists

of 20 equilateral triangles of equal size. In a first step, the root division step, the great circle arcs forming the edges of the basic triangles are divided into n equal arcs per edge (termed **Rn**). Connecting the new edge points by great-circle arcs yields n^2 spherical triangles within the original triangle. This step is followed by k bisection steps (termed **Bk**), where each triangle is recursively subdivided into 4 smaller triangles. This results in a so-called **RnBk** grid. The intermediate grids and the final grid are further optimized using spring dynamics (Tomita *et al.*, 2001), with the spring coefficient set to $\beta = 0.9$ in this work.* For a given resolution **RnBk**, the total number of cells n_c , edges n_e and vertices n_v can be computed from

$$n_c = 20n^2 4^k; \quad n_e = 30n^2 4^k; \quad n_v = 10n^2 4^k + 2. \quad (1)$$

In this article, the effective grid resolution $\overline{\Delta x}$ is defined as

$$\overline{\Delta x} = \sqrt{\overline{a_c}} = \sqrt{\frac{\pi}{5} \frac{r_e}{n^{2k}}}, \quad (2)$$

where $\overline{a_c}$ is the average cell area and r_e is the Earth's radius. Note that this definition differs from the average cell centre distances given in Wan *et al.* (2013), which are smaller by a factor of about $\sqrt{4/3}$ because a cell point has only three nearest neighbours on a triangular grid. In Table 1, some characteristics of commonly used grids are given, including the number of triangle cells and edges, the effective grid resolution and the area ratio of the largest to smallest triangles.

Table 1. Total number of cells and edges, effective grid resolution and area ratio of the largest to the smallest cells for grids referred to in this work.

Grid	Number of cells	Number of edges	Effective grid resolution (km)	Max/min cell area ratio
R2B04	20 480	30 720	157.8	1.38
R2B05	81 920	122 880	78.9	1.44
R2B06	327 680	491 520	39.5	1.49
R2B07	1 310 720	1 966 080	19.7	1.53

2.2. Model equations

The equation system of the ICON model is based upon the prognostic variables suggested by Gassmann and Herzog (2008), but uses the two-dimensional rather than the three-dimensional Lamb transformation to convert the nonlinear momentum advection into a vector-invariant form. So far, the shallow-atmosphere approximation has been applied, but there are plans to add an option for the unapproximated deep-atmosphere equations. The basic equation system reads as follows:

$$\frac{\partial v_n}{\partial t} + \frac{\partial K_h}{\partial n} + (\zeta + f)v_t + w \frac{\partial v_n}{\partial z} = -c_{pd}\theta_v \frac{\partial \pi}{\partial n} + F(v_n), \quad (3)$$

$$\frac{\partial w}{\partial t} + \mathbf{v}_h \cdot \nabla \mathbf{w} + w \frac{\partial w}{\partial z} = -c_{pd}\theta_v \frac{\partial \pi}{\partial z} - g, \quad (4)$$

$$\frac{\partial \rho}{\partial t} + \nabla \cdot (\mathbf{v}\rho) = 0, \quad (5)$$

$$\frac{\partial \rho \theta_v}{\partial t} + \nabla \cdot (\mathbf{v}\rho \theta_v) = \tilde{Q}. \quad (6)$$

*Optimizing the intermediate grids has little impact on the quality of the final grid, but it greatly speeds up the convergence of the grid optimization.

As in Gassmann (2013), Eq. (6) is reformulated using the time derivative of

$$\pi = \left(\frac{R_d}{p_{00}} \rho \theta_v \right)^{R_d/c_{vd}} \quad (7)$$

in order to obtain

$$\frac{\partial \pi}{\partial t} + \frac{R_d}{c_{vd}} \frac{\pi}{\rho \theta_v} \nabla \cdot (\mathbf{v} \rho \theta_v) = \hat{Q}, \quad (8)$$

which simplifies the implicit numerical treatment of the terms representing vertical sound-wave propagation. The prognostic variables of the (untransformed) equation system are the horizontal velocity component normal to the triangle edges v_n , the vertical wind component w , density ρ and virtual potential temperature θ_v . When coupled with moisture physics, ρ represents the full air density including liquid and solid hydrometeors. The reconstructed tangential velocity component is denoted as v_t and, in accordance with the model code, it is assumed here that (v_t, v_n, w) form a right-handed system. \mathbf{v}_h and \mathbf{v} denote the horizontal and three-dimensional wind vectors, respectively. The remaining symbols are the vertical vorticity component ζ , the Coriolis parameter f , the horizontal part of the kinetic energy $K_h = \frac{1}{2}(v_n^2 + v_t^2)$, the Exner function π , the specific heat capacities of dry air at constant pressure c_{pd} and volume c_{vd} , the gas constant of dry air $R_d = c_{pd} - c_{vd}$, the gravitational acceleration g and the reference pressure $p_{00} = 1000$ hPa conventionally used for defining the potential temperature. $\partial/\partial n$ denotes a horizontal derivative in the edge-normal direction, i.e. between the two adjacent mass points. Moreover, $F(v_n)$ denotes source terms for horizontal momentum (to be specified below) and \tilde{Q} and \hat{Q} denote appropriately formulated diabatic heat-source terms.

2.3. Spatial discretization

The spatial discretization of the above equations is performed on an icosahedral-triangular C grid. The mass points are located in the circumcentre of each triangular cell and the edge-normal horizontal velocity component is defined at the edge midpoints. Most of the basic horizontal operators are discretized in the same way as described by Wan *et al.* (2013) for the hydrostatic dynamical core. As detailed illustrations are provided there (see, in particular, fig. 1 in Wan *et al.*, 2013, for the arrangement of the variables), we will restrict ourselves here to a brief mathematical notation. The vertical discretization is formulated in a generalized height-based system that can, in principle, be specified according to the user's preferences. The default implementation uses the generalized smooth-level vertical coordinate described by Leuenberger *et al.* (2010), which is complemented by an automatic layer-thickness limiter that prevents too closely spaced (or even intersecting) model levels without any tuning efforts. As an alternative, the conventional Gal-Chen and Somerville (1975) formulation is available. Introducing some abbreviations for better readability, the discretized equation system reads

$$\frac{\partial v_n}{\partial t} + \text{adv}(v_n) = -c_{pd} \tilde{\theta}_v^e \text{grad}_h(\pi) + F(v_n), \quad (9)$$

$$\frac{\partial w}{\partial t} + \text{adv}(w) = -c_{pd} \left((\theta_0 + \bar{\theta}_v^i) \frac{\Delta \pi'}{\Delta z} + \bar{\theta}_v^i \frac{d\pi_0}{dz} \right), \quad (10)$$

$$\frac{\partial \rho}{\partial t} + \left[\frac{\tilde{\nabla} \cdot (\bar{v}_n^{\text{e-av}} \tilde{\rho}^e \Delta z^e) + \Delta((w - \bar{w}_{cc}^i) \tilde{\rho}^i)}{\Delta z} \right] = 0, \quad (11)$$

$$\begin{aligned} \frac{\partial \pi}{\partial t} + \frac{R_d}{c_{vd}} \frac{\pi}{\rho \theta_v} \\ \times \left[\frac{\tilde{\nabla} \cdot (\bar{v}_n^{\text{e-av}} \tilde{\rho}^e \tilde{\theta}_v^e \Delta z^e) + \Delta((w - \bar{w}_{cc}^i) \tilde{\rho}^i \tilde{\theta}_v^i)}{\Delta z} \right] = \hat{Q}, \end{aligned} \quad (12)$$

with

$$\text{adv}(v_n) = \frac{\Delta \bar{K}_h^c}{\Delta n} \Big|_s + v_t (\bar{\zeta}^e + f) + (w - \bar{w}_{cc}^i)^m \frac{\Delta \bar{v}_n^i}{\Delta z}, \quad (13)$$

$$\text{grad}_h(\pi) = \left(\frac{\Delta \pi'}{\Delta n} \Big|_s - \frac{\Delta h}{\Delta n} \Big|_s \frac{\Delta \bar{\pi}^i}{\Delta z} \right), \quad (14)$$

or, alternatively, the z -level horizontal pressure-gradient discretization described in Zängl (2012) and

$$\begin{aligned} \text{adv}(w) = & \left(\bar{v}_n^i \frac{\Delta w}{\Delta n} \Big|_s + \bar{v}_t^i \frac{\Delta \bar{w}^v}{\Delta t} \Big|_s \right) \\ & + (w - \bar{w}_{cc}^i) \frac{\Delta w}{\Delta z}. \end{aligned} \quad (15)$$

The averaging or interpolation operators used here are as follows:

- $(\cdot)^e$: a linear interpolation from cells or vertices to edges;
- $(\cdot)^c$: a bilinear interpolation from edges to cells;
- $(\cdot)^v$: an area-weighted interpolation from cells to vertices;
- $(\cdot)^i$: a linear interpolation from main levels to interface levels (quadratic extrapolation at the surface);
- $(\cdot)^m$: a linear interpolation from interface levels to main levels; and
- $(\cdot)^{\text{e-av}}$: a five-point velocity averaging operator needed to obtain a nearly second-order accurate discretization of divergence (see section A2).

Δ denotes a discretized differencing operator, which can be either a horizontal or a vertical gradient. Horizontal gradients in the edge-normal direction (denoted by n) are evaluated from the adjacent mass points and constitute nearly centred differences. An exception holds for the $\Delta \bar{K}_h^c / \Delta n$ term in Eq. (13), for which the three-point second-order accurate discretization Eq. (16) involving the adjacent mass points and the local edge point (at which the horizontal kinetic energy is computed in the first place) is used. For a generic variable ψ , it reads

$$\frac{\Delta \psi}{\Delta n} = \frac{l_{e,c1} \psi_{c2} - l_{e,c2} \psi_{c1} + \left(\frac{l_{e,c2}}{l_{e,c1}} - \frac{l_{e,c1}}{l_{e,c2}} \right) \psi_e}{l_d}, \quad (16)$$

where $l_{e,c1}$ and $l_{e,c2}$ are the distances between the edge point and the adjacent mass points of cells 1 and 2, respectively, and l_d is the distance between the two mass points (the so-called dual edge length). This special treatment has a beneficial impact on the wavenumber-five disturbances appearing, for instance, in the steady-state variant of the Jablonowski and Williamson (2006a) test. Horizontal gradients in the tangential direction (denoted by t) are evaluated from the adjacent vertices and constitute exact centred differences. Vertical gradients at main levels are exact centred differences, whereas vertical gradients at interface levels (in Eqs (10) and (15)) are not centred in the presence of vertical grid stretching. Therefore, the $\Delta w / \Delta z$ term in Eq. (15) uses a three-point second-order accurate discretization analogous to Eq. (16), involving the local point and the vertical neighbours. Moreover, h denotes the geometric height of a coordinate surface, $|_s$ indicates that a horizontal derivative is taken along a coordinate surface and θ_0 and π_0 refer to a reference atmosphere that allows for integrating the hydrostatic equation analytically, so that the required values can be obtained directly from analytical formulae. The specific formulation used here is the same as in Zängl (2012). The discretized tangential velocity v_t at the edge points is obtained from a four-point radial basis function (RBF) reconstruction following Narcovich and Ward (1994), using the edge points of the two triangles adjacent to the target point.

Extensive testing revealed that this particular reconstruction is very robust and insensitive against the RBF kernel and the scale factor. The contravariant correction ('cc') of the vertical wind speed w_{cc} is also defined at the edge points and given by

$$w_{cc} = v_n \frac{\Delta h}{\Delta n} + v_t \frac{\Delta h}{\Delta t}. \quad (17)$$

The vertical vorticity component ζ is defined on the vertices and is discretized using the Stokes theorem,

$$\zeta = \frac{1}{a_v} \sum_{i=1}^{n_e} v_n l_{df_o}, \quad (18)$$

where a_v is the area of the hexagonal/pentagonal dual cell centred at the vertex, n_e is the number of edges or cells adjacent to the vertex (usually 6, 5 at the 12 pentagon points of the basic icosahedron) and f_o is an orientation factor (± 1). Analogously, the discretized horizontal divergence operator $\tilde{\nabla}$ at the mass points is obtained from the Gauss theorem,

$$\tilde{\nabla}(\phi_e) := \frac{1}{a_c} \sum_{i=1}^3 \phi_e l_{pf_o}, \quad (19)$$

where ϕ_e represents a flux defined on edges, a_c is the area of the triangular cell and l_p is the primal edge length. Given the flux form of Eq. (11), this ensures local mass conservation to machine precision. In the absence of diabatic terms, $\rho\theta_v$ is conserved to machine precision as well (see the discussion after Eq. (31)). Finally, $\tilde{\psi}^e$ and $\tilde{\psi}^i$ denote upwind-biased reconstructions of a scalar variable ψ (representing ρ and θ_v) following the Miura (2007) scheme. To obtain a second-order accurate flux through a given edge, one first computes a backward trajectory with a length of $\frac{1}{2}\Delta t(v_t, v_n)$ starting at the edge. Then, starting from the upwind cell,

$$\tilde{\psi}^e = \psi_0^e + (\psi - \psi_0^e) + \nabla(\psi - \psi_0^e) \cdot \mathbf{d}(c, \text{tr}), \quad (20)$$

where ψ_0 denotes the reference-state value, $\nabla\psi$ is a first-order accurate horizontal gradient calculated with a four-point stencil using the Green–Gauss theorem and $\mathbf{d}(c, \text{tr})$ is the distance vector between the upwind cell point and the trajectory end point. The use of perturbation values for ρ and θ_v is motivated by the fact that an upwind-biased reconstruction of the full variables would not be consistent with the discretization of w_{cc} . As will be demonstrated with the Schär mountain test below, this inconsistency is mitigated by using analytical values for the height-related part of the ρ and θ_v gradients. A somewhat different discretization is chosen in the vertical direction, because it turned out that $\tilde{\psi}^i$ must be continuous at $w = 0$ in order to avoid spurious buoyancy waves. Starting from the local mass point at the interface level, we use

$$\tilde{\psi}^i = \bar{\psi}^i + \frac{\Delta\psi}{\Delta z} \cdot \mathbf{d}(i, \text{tr}) \quad (21)$$

where $\mathbf{d}(i, \text{tr})$ denotes the distance between the interface mass point and the end of the corresponding backward trajectory with a length of $\frac{1}{2}\Delta t(w - \overline{w_{cc}^i})$. The upper and lower boundary conditions applied in the numerical solution are $w = 0$ and $w = \overline{w_{cc}^i}$, respectively.

2.4. Temporal discretization

Time integration is accomplished with a two-time-level predictor–corrector scheme that is explicit except for the terms describing vertical sound-wave propagation. It has been recognized that time splitting in the sense of taking multiple acoustic substeps per dynamics time step, which is a widely

used approach in limited-area non-hydrostatic models, is not beneficial in a global model extending up to the stratopause region or even higher, because the ratio between the sound speed and the maximum wind speed tends to be too close to one. At spatial resolutions permitting breaking gravity waves in the mesosphere, local wind speed extrema in excess of 250 m s^{-1} have been encountered, which is difficult to verify due to the lack of detailed measurements but seems plausible from existing knowledge of gravity waves. In the ICON model, time splitting is applied instead between the dynamical core on the one hand and tracer advection, fast-physics parametrizations (e.g. turbulence, saturation adjustment and cloud microphysics) and horizontal diffusion on the other hand. The time-step ratio is usually chosen to be 4 or 5, based on a dynamics time step of $1.8 \times 10^{-3} \overline{\Delta x} \text{ s m}^{-1}$ (i.e. 1.8 times the value of $\overline{\Delta x}$ in units of km). Mass-consistent transport is achieved by passing time-averaged air-mass fluxes from the dynamical core to the transport scheme (to be described in a subsequent article; a brief overview is available from Lauritzen *et al.*, 2014). We anticipate here that a range of measures has been taken in the transport scheme to achieve the stability range required to accommodate our time-splitting approach. In the following description of the time-stepping scheme, the subscripts of the prognostic variables v_n and θ_v are dropped in order to use subscripts to denote the time level. Moreover, we combine $\theta = \theta_0 + \theta'$ in the vertical wind equation in order to simplify the notation.

• Predictor step:

$$\frac{v_{n+1*} - v_n}{\Delta t} + \text{adv}(v)_{n*} = -c_{pd} \tilde{\theta}_n^e \text{grad}_h(\pi)_{\bar{n}} + F_s(v), \quad (22)$$

$$\begin{aligned} \frac{w_{n+1*} - w_n}{\Delta t} + \text{adv}(w)_{n*} \\ = -c_{pd} \left[\tilde{\theta}_n^i \left(\beta_1 \frac{\Delta\pi'_{n+1*}}{\Delta z} + \beta_2 \frac{\Delta\pi'_n}{\Delta z} \right) + \tilde{\theta}_n^i \frac{d\pi_0}{dz} \right], \end{aligned} \quad (23)$$

$$\begin{aligned} \frac{\rho_{n+1*} - \rho_n}{\Delta t} + \frac{1}{\Delta z} \left[\tilde{\nabla} \cdot (\overline{v_{n+1*}^{e,av}} \tilde{\rho}_n^e \overline{\Delta z}^e) \right. \\ \left. + \Delta \{ (\beta_1 w_{n+1*} + \beta_2 w_n - \overline{w_{cc}^i}_{n+1*}) \tilde{\rho}_n^i \} \right] = 0, \end{aligned} \quad (24)$$

$$\begin{aligned} \frac{\pi_{n+1*} - \pi_n}{\Delta t} + \frac{R_d}{c_{vd}} \left(\frac{\pi}{\rho\theta} \right)_n \frac{1}{\Delta z} \left[\tilde{\nabla} \cdot (\overline{v_{n+1*}^{e,av}} \tilde{\rho}_n^e \tilde{\theta}_n^e \overline{\Delta z}^e) \right. \\ \left. + \Delta \{ (\beta_1 w_{n+1*} + \beta_2 w_n - \overline{w_{cc}^i}_{n+1*}) \tilde{\rho}_n^i \tilde{\theta}_n^i \} \right] = \hat{Q}. \end{aligned} \quad (25)$$

• Corrector step:

$$\begin{aligned} \frac{v_{n+1} - v_n}{\Delta t} + \gamma_1 \text{adv}(v)_{n+1*} + \gamma_2 \text{adv}(v)_{n*} \\ = -c_{pd} \tilde{\theta}_n^e \text{grad}_h(\pi)_{\bar{n}} + F_d(\mathbf{v})_{n+1*} + F_s(v), \end{aligned} \quad (26)$$

$$\begin{aligned} \frac{w_{n+1} - w_n}{\Delta t} + \gamma_1 \text{adv}(w)_{n+1*} + \gamma_2 \text{adv}(w)_{n*} \\ = -c_{pd} \left[(\delta_1 \tilde{\theta}_{n+1*}^i + \delta_2 \tilde{\theta}_n^i) \left(\beta_1 \frac{\Delta\pi'_{n+1}}{\Delta z} + \beta_2 \frac{\Delta\pi'_n}{\Delta z} \right) \right. \\ \left. + (\delta_1 \tilde{\theta}_{n+1*}^i + \delta_2 \tilde{\theta}_n^i) \frac{d\pi_0}{dz} \right], \end{aligned} \quad (27)$$

$$\begin{aligned} \frac{\rho_{n+1} - \rho_n}{\Delta t} + \frac{1}{\Delta z} \left[\tilde{\nabla} \cdot (\overline{v_{n+1}^{e,av}} \tilde{\rho}_n^e \overline{\Delta z}^e) \right. \\ \left. + \Delta \{ (\beta_1 w_{n+1} + \beta_2 w_n - \overline{w_{cc}^i}_{n+1**}) \right. \\ \left. \times (\delta_1 \tilde{\rho}_{n+1*}^i + \delta_2 \tilde{\rho}_n^i) \} \right] = 0, \end{aligned} \quad (28)$$

$$\begin{aligned} \frac{\pi_{n+1} - \pi_n}{\Delta t} + \frac{R_d}{c_{vd}} \left(\frac{\pi}{\rho \theta} \right)_n \frac{1}{\Delta z} \left[\tilde{\nabla} \cdot (\bar{v}_{n+1}^{c,av} \tilde{\rho}_n^c \tilde{\theta}_n^c \Delta z^c) \right. \\ \left. + \Delta \{ (\beta_1 w_{n+1} + \beta_2 w_n - \bar{w}_{cc}^{ci}) \right. \\ \left. \times (\delta_1 \tilde{\rho}_{n+1}^i + \delta_2 \tilde{\rho}_n^i) (\delta_1 \tilde{\theta}_{n+1}^i + \delta_2 \tilde{\theta}_n^i) \} \right] = \hat{Q}. \quad (29) \end{aligned}$$

Time-level indices n , $n+1^*$ and $n+1$ denote the current time level, the preliminary new time level resulting from the predictor time step and the new time level, respectively. The time level \tilde{n} , at which the horizontal pressure gradient is taken, is an extrapolated time level using levels n and $n-1$:

$$\pi_{\tilde{n}} := (1 + \alpha)\pi_n - \alpha\pi_{n-1}, \quad (30)$$

with α typically ranging between a third for mesh sizes smaller than about 40 km and two-thirds for very coarse resolutions. As revealed by the combined sound-wave-gravity-wave test developed by Baldauf *et al.* (2014), the extrapolation in time damps horizontally propagating sound waves without exerting a significant impact on gravity waves, which increases the numerical stability range with respect to evaluating the pressure gradient only at time level n . It can also be interpreted as an approximation of divergence damping by reformulating the terms $\sim \alpha$ as a time derivative of π and combining them with Eq. (8) (Klemp *et al.*, 2007). A very similar effect would be obtained by using time level n for the predictor step and an interpolated value between levels n and $n+1^*$ for the corrector step, but this would be computationally more expensive because the pressure gradient would then have to be evaluated twice as frequently. Note also that, for $\alpha = 0$, our scheme becomes essentially similar to the basic forward-backward scheme developed by Mesinger (1977).

The off-centring parameter β_1 (with $\beta_2 = 1 - \beta_1$) for the vertically implicit sound wave solver has a default value of 0.65, which is usually sufficient to ensure numerical stability in real-case applications with full physics coupling. The related parameter δ_1 (with $\delta_2 = 1 - \delta_1$) for $\tilde{\rho}^i$ and $\tilde{\theta}^i$ has a default value of 0.4, which has been found to optimize the numerical stability for combinations of coarse horizontal resolution (mesh sizes of 100 km or more) with very high model tops (75 km or more). In dynamical core tests considering sound wave propagation, like that proposed by Baldauf *et al.* (2014), $\alpha = 0$, $\beta_1 = 0.5$ and $\delta_1 = 0.5$ deliver the closest agreement with the analytical solution, with the caveat that non-zero large-scale winds require β_1 to be slightly larger than 0.5 in order to avoid numerical instabilities near the pentagon points of the icosahedron. Note that, for efficiency reasons, $\bar{\rho}^i$ and $\bar{\theta}^i$ are used instead of $\tilde{\rho}^i$ and $\tilde{\theta}^i$ in the predictor step. The impact of this optimization on the quality of the results was found to be negligible. Horizontal momentum advection at the predictor step is reused from the corrector step of the preceding time step (n^*), whereas an interpolation between time levels n^* and $n+1^*$ with $\gamma_1 = 0.75$ and $\gamma_2 = 1 - \gamma_1$ is used in the corrector step. The impact of this tuning measure on numerical stability is rather small, but is noticeable in situations with large-amplitude breaking gravity waves. Using time level n instead of n^* , which requires calculating the momentum advection terms twice per time step, is available as an option but does not seem to give any added value. Moreover, time level $n+1^{**}$ for the w_{cc} term means that, by default, time level $n+1^*$ is used in the predictor and corrector steps, but an option for recalculating the term at time level $n+1$ in the corrector step is available. The latter potentially improves numerical stability under extreme conditions, but has been found to be important only at horizontal mesh sizes of less than about 1 km and slope angles exceeding 60°.

For the numerical implementation, this implies that, in both substeps (predictor and corrector), the horizontal momentum equation and the advection part of the vertical momentum equation are calculated first. The updated v is then used for computing the horizontal flux divergences in the continuity and Exner pressure equations. The remaining terms are part of the

vertically implicit solution, which is calculated with a standard algorithm for three-band matrices. After the update of ρ and π , θ_v is recalculated using the linearized state equation

$$\theta_{n+1} = \theta_n \frac{\rho_n}{\rho_{n+1}} \left[1 + \frac{c_{vd}}{R_d} \left(\frac{\pi_{n+1}}{\pi_n} - 1 \right) \right], \quad (31)$$

which follows the method proposed by Gassmann (2013) and provides exact conservation of $\rho\theta_v$ (in the absence of diabatic terms), although a prognostic equation for π is solved in the first place. As pointed out by one of the reviewers, this procedure may be interpreted as solving two prognostic thermodynamic equations with self-consistent tendency terms, contrasting with the usual way of solving one prognostic equation and applying the diagnostic state equation (7). In fact, using Eq. (7) instead of Eq. (31) would not conserve $\rho\theta_v$, even though the (relative) conservation errors found in dedicated tests were only of order 10^{-8} and thus probably too small to be noticeable in real-case applications with physics parametrizations.

The external forcing terms $F_s(v)$ and \hat{Q} represent momentum and (properly converted) temperature tendencies from slow-physics parametrizations (e.g. convection and radiation). Fast-physics parametrizations, which are called at every physics time step (e.g. saturation adjustment, cloud microphysics and turbulence), sequentially update the prognostic variables (operator splitting) and therefore do not provide tendencies to the dynamical core. $F_d(v)$ in Eq. (26) represents a fourth-order divergence damping term, which has been introduced in order to allow calling of the (computationally more expensive) diffusion operator (see below) at the physics time steps only without incurring numerical stability problems under extreme conditions:

$$F_d(v) = -f_d \bar{a}_c^{-2} \nabla \tilde{\nabla} \cdot \left(\nabla \left[\tilde{\nabla} \cdot v + \frac{\Delta}{\Delta z} \left(w - \bar{w}_{cc}^{ci} \right) \right] \right). \quad (32)$$

f_d typically attains values between $1/(1000\Delta t)$ and $1/(250\Delta t)$ and \bar{a}_c is the global mean cell area. For the standard time step mentioned above, this corresponds to hyperviscosities between 0.55 and $2.2 \bar{\Delta x}^3 \text{ m}^4 \text{ s}^{-1}$, where $\bar{\Delta x}$ has to be inserted in units of m. Systematic tests have revealed that the divergence damping starts to exert a detectable impact on the kinetic energy spectrum at about $1/(500\Delta t)$. In addition, it has been found that higher values than $1/(500\Delta t)$ are usually needed in the upper stratosphere and the mesosphere in order to prevent numerical instabilities in breaking gravity waves, and in the presence of mountain slopes steeper than about 60°. We therefore impose a height-dependent lower limit on f_d that increases linearly from zero to $1/(250\Delta t)$ between 20 and 40 km and then remains constant for larger heights.

Another optional artificial damping term, which is not included in the above equations, is Rayleigh damping on w following Klemp *et al.* (2008), which serves to prevent unphysical reflections of gravity waves at the model top. Deviating from the original proposal by Klemp *et al.* (2008), the vertical profile of the damping coefficient used in ICON is given by a hyperbolic tangent rather than a \sin^2 because this turned out to yield even less wave reflection for a given damping layer depth.

2.5. Horizontal diffusion

For horizontal numerical diffusion of horizontal momentum, two distinctly different alternatives are available. The first one is a purely computational fourth-order diffusion, using the same discretization as described by Wan *et al.* (2013) for the hydrostatic dynamical core. As we need to distinguish between normal and tangential velocity components below, we here resume denoting them as v_n and v_t , respectively:

$$F_D(v_n) = -K_4 \nabla^2 [\nabla^2(v_n)], \quad (33)$$

with

$$\nabla^2(v_n) = \nabla \tilde{\nabla} \cdot v_n - \nabla_t \zeta, \quad (34)$$

where ∇_t denotes a tangential gradient taken between the two vertices adjacent to an edge and a_e is the area represented by an edge. While this discretization effectively damps small-scale noise, it has the disadvantages of not converging against the analytical operator (Wan, 2009) and of generating wavenumber-five disturbances when applied with a diffusion coefficient sufficiently large to reliably prevent energy accumulation at the two-delta scale in real-case set-ups with full physics coupling. This option has been retained for reference, but is not used in standard applications.

Our default approach is a more physically motivated second-order Smagorinsky diffusion of velocity and potential temperature combined with a fourth-order background diffusion of velocity, using a different discretization for velocity that is formally second-order accurate on equilateral triangles. The latter starts with an RBF reconstruction of the two-dimensional wind vector at the triangle vertices and then applies the conventional centred-difference stencil for the second derivative (keeping in mind the caveats that for spherical triangles the differences in the edge-normal direction may not be centred and the line connecting the outer vertices may not intersect the edge at a right angle). Similarly, (approximately) centred differences are used for computing the horizontal deformation of the wind field (see Figure 1 for explanation of symbols):

$$F_{D2}(v_n) = 4K_h \tilde{\nabla}^2(v_n), \quad (35)$$

with

$$\tilde{\nabla}^2(v_n) = \frac{v_{n2} + v_{n1} - 2v_n}{l_p^2} + \frac{v_{n4} + v_{n3} - 2v_n}{l_{vv}^2} \quad (36)$$

and

$$K_h = f_s a_e \left[\left(\frac{v_{n4} - v_{n3}}{l_{vv}} - \frac{v_{t2} - v_{t1}}{l_p} \right)^2 + \left(\frac{v_{n2} - v_{n1}}{l_p} + \frac{v_{t4} - v_{t3}}{l_{vv}} \right)^2 \right]^{1/2} \quad (37)$$

(the factor of 4 in Eq. (35) comes from the lengths in the denominator of Eq. (36) being twice those needed for the diffusion stencil). The scaling factor f_s , corresponding to the square of the Smagorinsky constant c_s , has a default value of 0.015. The value of f_s needed for numerical stability depends on whether a parametrization for turbulent vertical mixing is used or not. If yes (e.g. in real-case applications with full physics coupling), a value of 0.005 is already sufficient for numerical stability, even

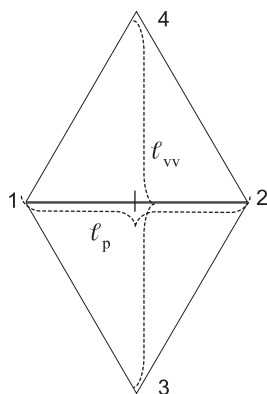


Figure 1. Illustration of the symbols used in Eqs (36) and (37).

though the skill scores tend to be better with somewhat stronger dissipation. In pure dynamical core tests involving a strong energy cascade towards small scales (e.g. the Jablonowski and Williamson (2006a) baroclinic wave test), f_s should not be smaller than our default of 0.015. Smagorinsky diffusion of potential temperature is formulated as

$$F_{D2}(\theta) = a_c \tilde{\nabla} \cdot \left(K_h \frac{\Delta \theta}{\Delta n} \right). \quad (38)$$

The metric correction terms related to the coordinate transformation are (currently) not included in the discretization of the diffusion terms for pragmatic reasons. Most importantly, accounting for the metric terms reduces the Courant-Friedrichs-Lewy (CFL) stability limit of K_h by a factor of approximately $(\Delta h / \Delta z)^2$, requiring an unreasonably strong limitation of K_h when $\Delta h / \Delta z$ exceeds a value of a few tens (unless using an implicit solver for the diffusion equation, which is not straightforward to implement for horizontal diffusion). The systematic errors induced by neglecting the metric terms are usually small for momentum diffusion because the effect of surface friction follows the surface and thus the terrain-following coordinates. For (potential) temperature, however, systematic errors in steep mountain valleys can potentially be substantial, because diffusion along terrain-following coordinate surfaces tends to dissolve low-level cold-air pools (see Zängl, 2002). In the ICON implementation, this issue is tolerable due to the absence of a background diffusion of temperature.

The fourth-order background diffusion is discretized as

$$F_{D4}(v_n) = -k_4 a_e^2 \tilde{\nabla}^2[\tilde{\nabla}^2(v_n)]. \quad (39)$$

If it is applied, an (empirically determined) offset of $0.75k_4 a_e$ is subtracted from K_h in Eq. (35) in order to avoid excessive diffusion under weakly disturbed conditions. We mention that the background diffusion is not needed for numerical stability, because the above-mentioned divergence damping is sufficiently strong to control noise at the two-delta scale. Practical experience has revealed, however, that a weak fourth-order background diffusion with a damping time-scale (with respect to two-delta waves) of the order of $60\text{--}120\Delta t$ has a beneficial impact on the disturbances developing in atmosphere-at-rest tests over real (global) orography. This corresponds to hyperviscosities of $0.07\text{--}0.14 \overline{\Delta x}^3 \text{ m}^4 \text{ s}^{-1}$, with $\overline{\Delta x}$ inserted in units of m. Moreover, the offset has the positive side effect that the Smagorinsky temperature diffusion is usually inactive under weak-wind conditions, which prevents detrimental impact on stable layers in mountain valleys even when a weak thermally driven circulation is present. The background diffusion is therefore used by default, but can be turned off for testing.

A fourth-order computational diffusion is also available for vertical wind speed. It has basically no impact on the model results at spatial resolutions within the validity range of a hydrostatic model, but the filter term is needed at resolutions of $\mathcal{O}(1 \text{ km})$ or finer because the advection of vertical wind speed has no implicit damping of small-scale structures. As will be shown below, it solves a problem encountered in an earlier publication (Zängl, 2012), where the vertical wind diffusion was not yet implemented. It is formulated as

$$F_D(w) = -k_w a_e^2 \nabla^2[\nabla^2(w)], \quad (40)$$

with

$$\nabla^2(w) = \tilde{\nabla} \cdot \frac{\Delta w}{\Delta n}. \quad (41)$$

The damping time-scale (with respect to two-delta waves) typically ranges between 15 and $50\Delta t$, the former value being needed in the presence of slope angles significantly exceeding 60° .

The corresponding values of hyperviscosity range between 0.17 and $0.55 \overline{\Delta x}^3 \text{ m}^4 \text{ s}^{-1}$, with $\overline{\Delta x}$ inserted in units of m.

As already mentioned, all diffusion terms are called at the physics time step. Diffusion is called right after the last dynamics time step before entering the physics interface and acts on the variables at the most recent time level $n + 1$. All variables on which diffusion is applied are updated directly, with π being recalculated from θ_v under the condition that density remains unchanged, so that the fields entering the physics interface are already horizontally filtered.

2.6. Physics–dynamics coupling

While a detailed description of the physics–dynamics coupling is beyond the scope of this article, a few important aspects will be anticipated here. The physics–dynamics coupling in ICON differs from many existing atmospheric models in that it is performed at constant density (volume) rather than constant pressure. This is related to the fact that the total air density ρ is one of the prognostic variables, whereas pressure is only diagnosed for parametrizations needing pressure as an input variable. Thus, it is natural to keep ρ constant in the physics–dynamics interface (corrections accounting for parametrized vertical moisture transports, e.g. surface moisture fluxes or hydrometeor sedimentation, have not yet been included at the time of writing this article). As a consequence, heating rates arising from latent heat release or radiative flux divergences have to be converted into temperature changes using c_v , the specific heat capacity at constant volume of moist air. Some physics parametrizations inherited from hydrostatic models, in which the physics–dynamics coupling always assumes constant pressure, therefore had to be adapted appropriately. Moreover, it is important to note that the diagnosed pressure entering into a variety of parametrizations is a hydrostatically integrated pressure rather than a non-hydrostatic pressure derived directly from the prognostic model variables. This is motivated by the fact that the pressure is generally used in physics schemes to calculate the air mass represented by a model layer and necessitated by the fact that sound waves generated by the saturation adjustment can lead to a local pressure increase with height in very extreme cases, particularly between the lowest and the second lowest model levels.

For efficiency reasons, a distinction is made between so-called fast-physics processes, which are always calculated at every physics time step, and slow-physics processes, which may be called at longer time steps (specified by the user) and provide tendencies to the dynamical core that remain constant between two successive calls of the parametrization. Fast-physics processes are treated with operator splitting, which means that (with exceptions noted below) they act on an atmospheric state that has already been updated by the dynamical core, horizontal diffusion and tracer transport scheme. Each process then sequentially updates the atmospheric variables and passes a new state to the subsequent parametrization. The calling sequence is saturation adjustment, surface transfer scheme, land-surface scheme, boundary-layer/turbulent vertical diffusion scheme, microphysics scheme and again saturation adjustment, in order to enter the slow-physics parametrizations with an adjusted state. The exceptions from the above-mentioned operator splitting are the surface-transfer scheme and the land-surface scheme, which take the input at the ‘old’ time level because the surface variables are not updated in the dynamical core and the surface-transfer coefficients and fluxes would be calculated from inconsistent time levels otherwise.

Another important aspect is related to the fact that physics parametrizations traditionally work on mass points (except for three-dimensional turbulence schemes). While the conversion between different sets of thermodynamic variables is reversible (except for numerical truncation errors), the interpolation between velocity points and mass points potentially induces errors. To minimize them, the velocity increments, rather than

the full velocities, coming from the turbulence scheme are interpolated back to the velocity points and then added to the prognostic variable v_n .

2.7. Physics parametrization package for operational NWP

For completeness, we mention here the physics parametrizations envisaged for operational NWP at DWD. The fast-physics parametrizations have been inherited from the operational regional COSMO model (Doms and Schättler, 2004), except for the saturation adjustment, which had to be reformulated for ICON due to the above-mentioned constant-volume coupling. The cloud microphysics scheme is a slightly extended version of the COSMO-EU five-category prognostic scheme (Doms and Schättler, 2004; Seifert, 2008), the most important modification being the inclusion of cloud ice sedimentation. The turbulence scheme (Raschendorfer, 2001) is based on a prognostic equation for turbulent kinetic energy (TKE) and has undergone some revision for ICON in order to improve the numerical stability under extreme conditions. Moreover, the TERRA land-surface scheme (Heise *et al.*, 2006) has recently been extended with a multilayer snow scheme and an option for a tile-based approach accounting for subgrid-scale land-cover variability. The slow-physics parametrizations have mostly been imported from the Integrated Forecasting System (IFS) of the European Centre for Medium-Range Weather Forecasts (ECMWF). Specifically, we use the Bechtold *et al.* (2008) convection scheme, the Lott and Miller (1997) subgrid-scale orography scheme and the Orr *et al.* (2010) non-orographic gravity-wave drag scheme. In addition, the Rapid Radiation Transfer Model (RRTM) radiation scheme (Mlawer *et al.*, 1997) is used in a similar version to that in the IFS.

3. Results of validation tests

To demonstrate the functionality and the quality of the dynamical core described in the preceding section, results from a hierarchy of tests of varying complexity will be presented in the following. In addition, we refer the reader to the sound-wave–gravity-wave test of Baldauf *et al.* (2014), where the ICON dynamical core is shown to achieve second-order convergence against the analytical solution derived in that work, provided that the above-mentioned damping mechanisms for sound waves (section 2.4) are turned off.

3.1. Jablonowski–Williamson test

We start with the Jablonowski and Williamson (2006a) test, denoted as JW test in the following, which is nowadays considered as a standard test for dynamical cores in global models. It consists of two configurations, differing in whether or not an initial perturbation is specified in order to trigger baroclinic waves. The basic state is a zonally symmetric, strongly baroclinic atmosphere with a surface Equator-to-Pole temperature contrast of about 80 K. It is in hydrostatic and geostrophic balance and therefore should remain stationary for all times if no perturbation is imposed. In practice, only models formulated in spherical harmonics or on a (non-rotated) latitude–longitude grid, which exactly allow representation of the symmetries of the analytical initial state, are able to maintain the initial state, because any disturbance initiated by grid irregularities tends to grow exponentially with time in the baroclinic environment. The so-called steady-state JW test therefore allows assessment of the presence and magnitude of grid imprinting of a numerical model. In the JW baroclinic wave test, a weak (and unbalanced) perturbation is imposed on the initial wind field at 20°N, 40°E. The perturbation grows very slowly during the first few days, but evolves into an explosive cyclogenesis between days 7 and 10 of the test case. At coarse mesh sizes resolving the baroclinic waves only marginally, this test highlights the diffusivity (or effective

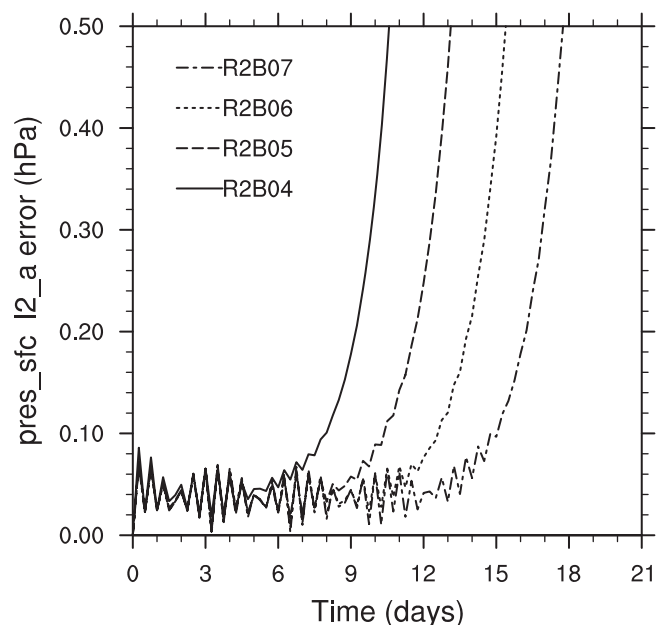


Figure 2. Temporal evolution of the L2 error of surface pressure (hPa) for model grids ranging from R2B04 (160 km) to R2B07 (20 km).

resolution) of a dynamical core and the presence of phase-speed errors in the advection of poorly resolved structures.

The results of the steady-state JW test are summarized in Figure 2, showing the temporal evolution of the L2 error of surface pressure for model grids ranging from R2B04 (160 km) to R2B07 (20 km). Following Lauritzen *et al.* (2010), an L2 error of 0.5 hPa is considered as the threshold beyond which the initial state is considered as broken. According to this measure, the steady state is kept for about 10.5 days at a mesh size of 160 km and for nearly 18 days at a mesh size of 20 km. For each factor-of-2 refinement of the model resolution, the initial state is maintained for about 2.5 days longer. Note that this constitutes a significant improvement over the hydrostatic ICON dynamical

core, for which the 0.5 hPa threshold was already reached after about 10 days at a mesh size of 105 km (fig. 12 in Lauritzen *et al.*, 2010). It is mentioned that the high-frequency oscillations visible during the initial phase before the onset of the exponential error growth are related to gravity waves that are excited due to inaccuracies in the specification of the initial state. While an exact analytical specification of the initial state is available for hydrostatic models using a pressure-based sigma coordinate, an iterative procedure is needed for non-hydrostatic models using a height-based coordinate. However, no special efforts have been made to minimize these initial gravity waves, because they do not seem to affect the results of interest adversely.

For the baroclinic wave test, Figure 3 displays the surface pressure and the relative vorticity ζ at 850 hPa after 9 days of simulation. The results can be compared with figs 7 and 9 of Wan *et al.* (2013) for the hydrostatic dynamical core. In accordance with those, it can be seen that the core pressure of the two main cyclones is not as low for R2B04 as for the higher resolutions, whereas the leftmost cyclone is somewhat deeper. The latter is likely a side effect of grid imprinting, providing an additional triggering mechanism for cyclogenesis. Moreover, a phase error can be noticed for R2B04, with the middle and left cyclones being located farther west than for the higher resolutions. This corresponds to too slow a propagation speed. The phase lag is, however, not as large as for the hydrostatic core. Taking the location of the cyclone centres at R2B07 as a reference, the phase lag of the left and middle cyclones is about 30% less than for the hydrostatic core. Moreover, the position of the deepest (right) cyclone is unbiased within the accuracy of detection whereas a phase lag of about 2° longitude can be diagnosed for the hydrostatic core. This improvement is most likely related to the fact that a second-order upwind finite-volume scheme is used for computing the horizontal fluxes of ρ and θ_v in the non-hydrostatic core (see section 2.3), whereas second-order centred differences, which are known to suffer from larger numerical dispersion errors, are used in the hydrostatic core for the corresponding computations. Comparison with further references can be made using the error metric defined by Jablonowski and Williamson (2006a,b), i.e. the zonal shift minimizing the L2 error against the

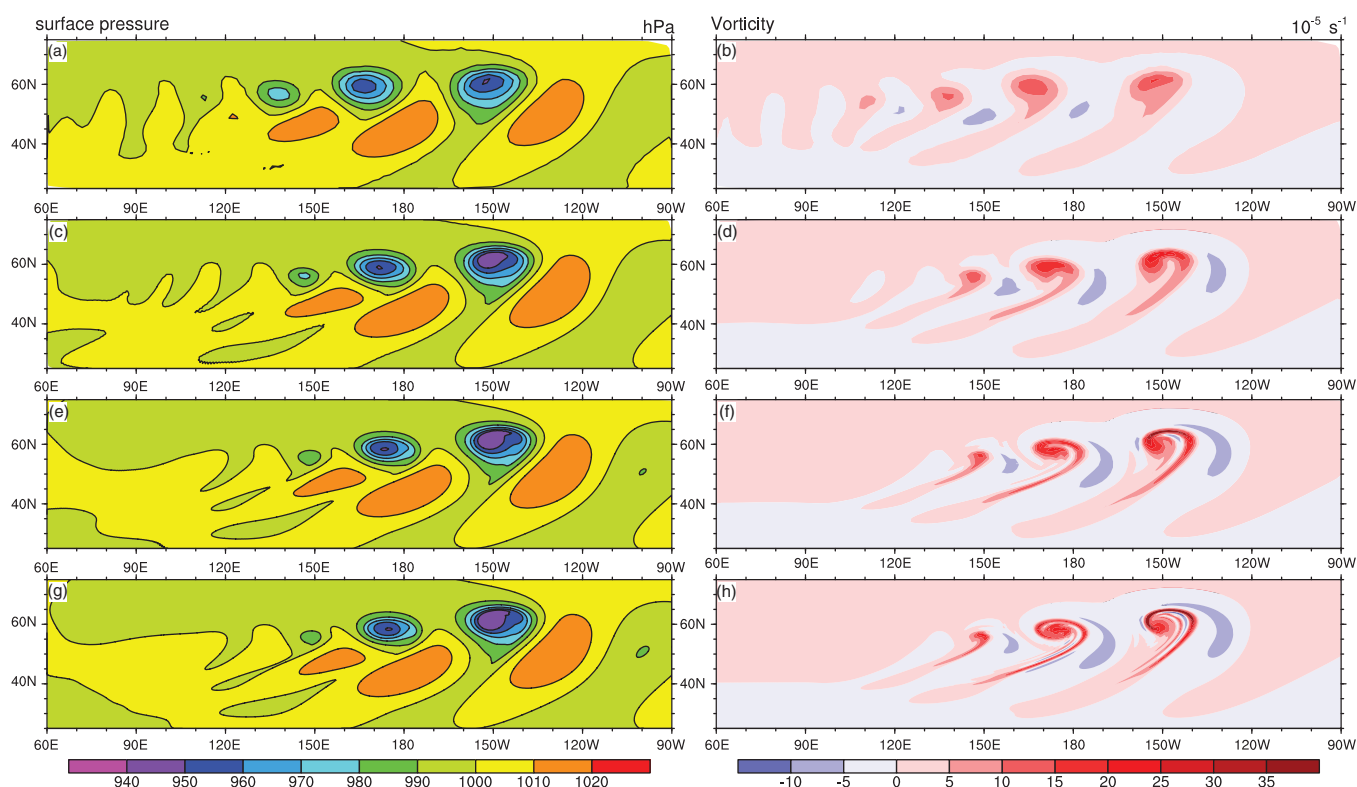


Figure 3. Surface pressure (hPa) and relative vorticity ζ at 850 hPa (10^{-5} s^{-1}) after 9 days of simulation for model grids of (a, b) R2B04, (c, d) R2B05, (e, f) R2B06 and (g, h) R2B07, corresponding to average mesh sizes of 160, 80, 40 and 20 km, respectively.

high-resolution solution. This metric yields a day-9 phase lag of 4° for R2B04, which has the same number of velocity points as the hexagonal grids considered in fig. 14 in Skamarock and Gassmann (2011), and a phase lag of 7° for R3B03 (not shown), which has a comparable number of mass points. The comparison indicates that the phase lag errors are smaller than for the hexagonal A-grid GME, even when keeping the number of mass points the same, whereas a quality comparable to hexagonal C grid models (using second-order accurate discretizations) is achieved when the total number of degrees of freedom (mass points plus velocity points) is kept fixed.

For comparing the ζ fields with other references, it has to be noted that for convenience of plotting –to make use of the built-in interpolation to pressure levels– ζ has first been interpolated from vertices to cells. Thus, the ζ fields look smoother and show somewhat smaller extrema than those in Wan *et al.* (2013). Apart from that, the reduction of the phase lag compared with the hydrostatic core is confirmed and, at the higher resolutions, some of the filamentary structures along the frontal zones are more pronounced than for the hydrostatic core, despite the above-mentioned vertex-to-cell interpolation, most likely because the amount of numerical diffusion applied here is less than for the hydrostatic core. Moreover, a non-understood instability evolving in the hydrostatic core (fig. 9 in Wan *et al.*, 2013) in the right cyclone does not appear here.

3.2. Schär mountain test

To check whether the metric terms related to the terrain-following coordinate transformation are discretized in a consistent manner, a test introduced by Schär *et al.* (2002), nowadays known as the Schär mountain test case, has been conducted. The test is originally two-dimensional and considers uniform flow with constant wind speed U and Brunt–Väisälä frequency N over a sequence of mountains defined by

$$h(x) = h_m \exp\left(-\frac{x^2}{a^2}\right) \cos^2 \frac{\pi x}{\lambda}. \quad (42)$$

With the usual parameter settings, $h_m = 250$ m, $a = 5000$ m, $\lambda = 4000$ m, $N = 10^{-2} \text{ s}^{-1}$ and $U = 10 \text{ m s}^{-1}$, the mountain triggers a combination of small-scale, rapidly decaying non-hydrostatic gravity waves and a larger-scale, quasi-hydrostatic vertically propagating gravity wave. The latter tends to exhibit perturbations reflecting the structure of the small-scale mountains if the model equations are not discretized consistently. Here, the test has been conducted in a quasi-three-dimensional mode, using a mountain ridge having constant height in the y -direction over a distance of 100 km and then gradually decaying to zero. The

model grids used for our test have been constructed starting from the global icosahedron by successive refinement of limited-area subdomains down to the desired target mesh sizes. The grids are therefore not aligned with the orientation of the mountain ridge, posing an additional challenge to the accuracy of the discretization. The model top is located at a height of 40 km and the Rayleigh damping on w (see section 2.4) that is needed to prevent the unwanted reflection of gravity waves starts at a height of 27.5 km. Results after 12 h of integration are shown in Figure 4 for mesh sizes of 625 and 312 m, respectively. They can be compared against the linear analytical solution (Schär *et al.*, 2002) and results from other numerical models, usually published for a mesh size of 500 m (Schär *et al.*, 2002; Klemp and Skamarock, 2003; Skamarock *et al.*, 2012). It is evident, that despite using an irregular spherical grid, no suspicious structures are generated over the mountain even at the coarser resolution. Both results compare favourably with the analytical solution and there are only slight differences in the wave amplitude between $\Delta x = 625$ m (Figure 4(a)) and $\Delta x = 312$ m (Figure 4(b)), indicating that resolving the peak-to-peak distance λ of 4000 m with about six grid points is already sufficient for an accurate representation of the flow structure.

3.3. Flow over very steep mountains

As already indicated in section 2.5, two of the experiments of Zängl (2012) are repeated here in order to document that a numerical deficiency that remained open in this earlier publication has been solved in the meantime. The tests consider the flow of an isothermal atmosphere with $U = 20 \text{ m s}^{-1}$ over a circular Gaussian mountain:

$$h(x, y) = h_m \exp\left(-\frac{x^2 + y^2}{a^2}\right), \quad (43)$$

with $a = 2000$ m and $h_m = 4000$ and 7000 m, respectively. The maximum slope of these mountains is about 1.7 and 3, respectively, corresponding to slope angles of 59° and 71° . The ICON non-hydrostatic dynamical core remains numerically stable in the presence of such steep mountains, thanks to the z -level horizontal pressure-gradient discretization described in Zängl (2012), but the results shown in Figure 5(c) and (d) of that study exhibited unexpected, nearly vertically oriented structures of vertical motion over the mountain that were believed to be numerical artefacts. These allegedly spurious vertical motions were weak but noticeable for the 4000 m mountain and attained maxima of more than 5 m s^{-1} for the 7000 m mountain. The updated results displayed in Figure 5 show that for the 4000 m mountain, not even weak indications of numerical artefacts are

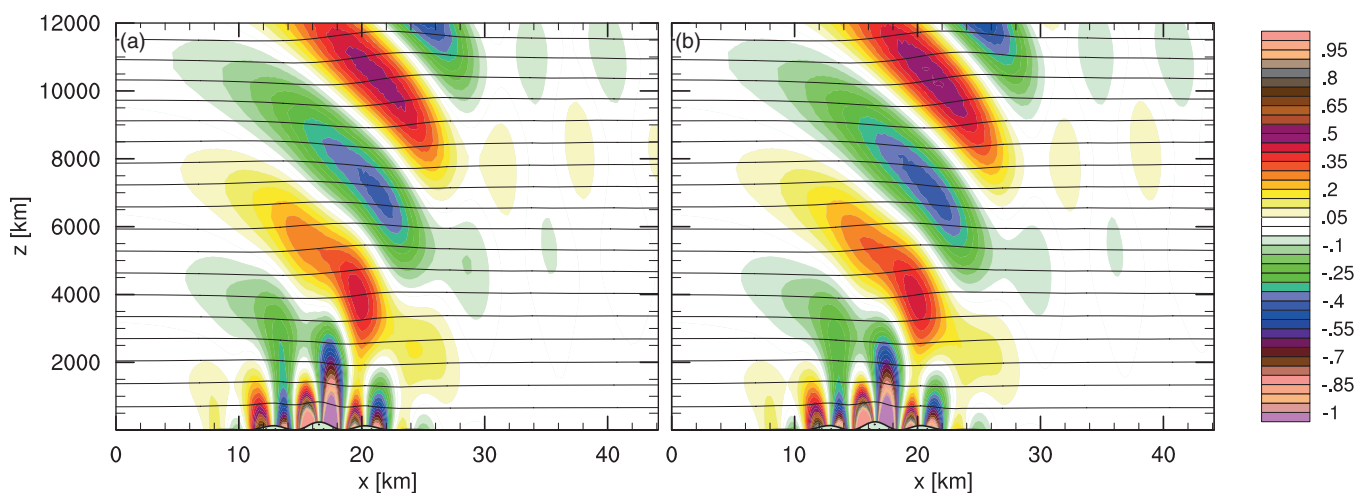


Figure 4. Vertical velocity (shading increment 0.05 m s^{-1} , see colour key) and potential temperature (contour interval 2 K) for the Schär *et al.* (2002) mountain wave test after 12 h of integration, using mesh sizes of (a) $\Delta x = 625$ m and (b) $\Delta x = 312$ m.

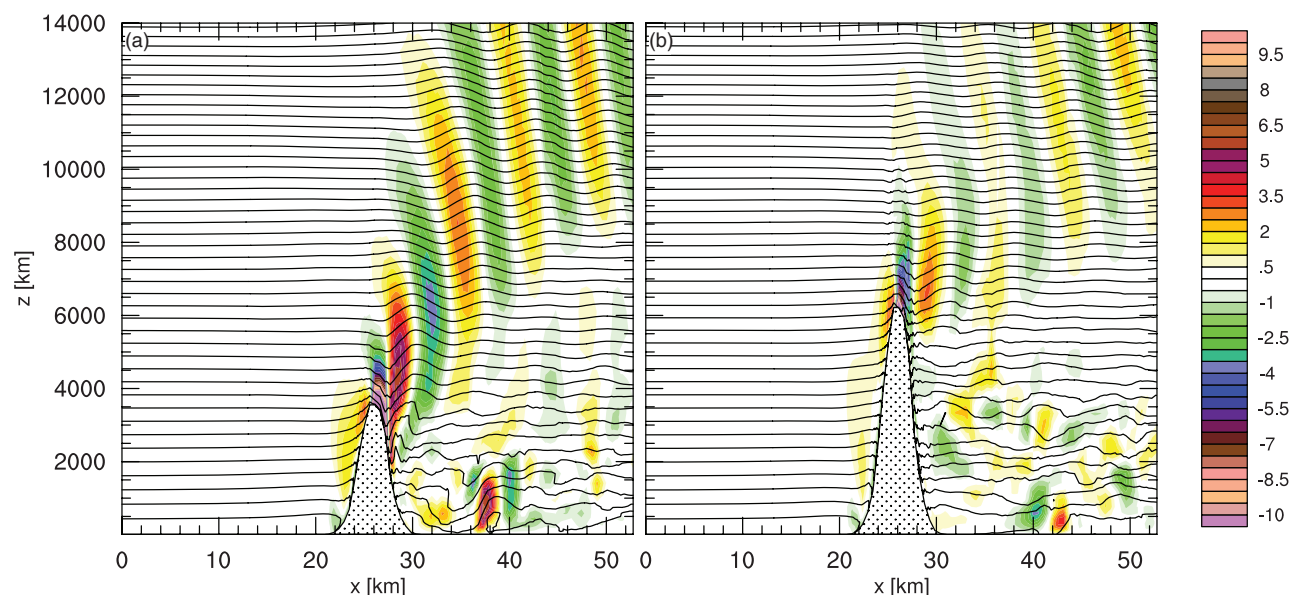


Figure 5. Vertical velocity (shading increment 0.5 m s^{-1} , see colour key) and potential temperature (contour interval 4 K) after 6 h of integration for flow over a circular Gaussian mountain (see text for details). Mountain heights are (a) 4000 m and (b) 7000 m.

visible over the mountain (Figure 5(a)), whereas the 7000 m mountain now approximately demarcates the threshold at which spurious motions and noisy isentropes start to become evident (Figure 5(b)). Moreover, unlike the earlier results, the gravity-wave activity is significantly weaker for the 7000 m mountain than for the 4000 m mountain, as expected from the fact that the flow regime should transition more and more towards a flow around the mountain for non-dimensional mountain heights above 5 (Smith, 1989). As already mentioned in section 2.5, the lack of numerical filtering of vertical wind speed was one of the reasons for the problems encountered before. Another contribution stems from changing the computation of vertical fluxes of ρ and θ , from centred differences to a second-order upwind scheme (see Eq. (21)). Note, in addition, that the scaling factors for the divergence damping and the Smagorinsky diffusion, f_d and f_s , had to be increased to $1/(250\Delta t)$ and 0.025, respectively, in order to prevent small-scale noise or even numerical instabilities for the 7000 m mountain. These are still reasonable values, but we nevertheless recommend avoiding slope angles close to or even above 70° in scientific applications.

3.4. Weisman–Klemp supercell test

Due to the strongly nonlinear behaviour of moist dynamics, validating the correctness of the coupling between the dynamical core, tracer advection, saturation adjustment and cloud microphysics is much more difficult than validating a dry dynamical core and in a strict sense not possible at all. One test that is frequently used to achieve some confidence in a newly developed model considers the development of a pair of supercells following the Weisman and Klemp (1982) set-up. The atmospheric environment prescribed in this test is conditionally unstable, with CAPE values in excess of $1000 \text{ m}^2 \text{ s}^{-2}$, and a strong low-level wind shear provides the vorticity for the development of supercell storms. Here we use an asymptotic wind speed of 25 m s^{-1} and a surface specific humidity of 14 g kg^{-1} , which yields a CAPE value of about $2200 \text{ m}^2 \text{ s}^{-2}$ and thus a theoretical upper limit of w (disregarding mixing and water loading) of about 66 m s^{-1} . The warm bubble specified to initiate the storm development follows the setting of Weisman and Klemp (1982). To be consistent with previous studies, a simple Kessler-type (warm-rain only) cloud microphysics scheme is used (accounting for the ice phase provides additional latent heat release and thus higher vertical wind speeds). The horizontal mesh sizes considered in the following, 1.25 km and 625 m, are finer than the 2 km used in the original work, which nowadays is known to be too coarse to

resolve the convective updraughts adequately (Bryan *et al.*, 2003). As above, non-uniform limited-area grids constructed from the global icosahedron have been used.

Selected results after 2 h of simulation are displayed in Figure 6. The surface precipitation field (Figure 6(a)) of the 625 m run shows the expected signature of a pair of supercell storms moving to the left and right of the wind shear vector, respectively. The precipitation field obtained for 1.25 km mesh size (not shown) differs only in minor details. In either case, there is no exact left–right symmetry, because an irregular spherical grid has been used for the simulation. The maximum rainfall amount is close to 40 kg m^{-2} for both resolutions. The time series of maximum vertical wind speed (Figure 6(b)) indicate peak values around 45 m s^{-1} for a mesh size of 1.25 km and slightly above 50 m s^{-1} for a mesh size of 625 m. This is, as expected, more than the maxima recorded in the original work (about 30 m s^{-1}), but in the same range as more recent references (e.g. Weisman and Rotunno, 2000).

3.5. Kinetic energy spectra

Energy spectra, depicting the spectral distribution of kinetic energy against the spherical wave number k , are an important measure to evaluate the effective resolution of a numerical model. From observations (Nastrom and Gage, 1985; Lindborg, 1999), it is known that the energy spectrum should scale as k^{-3} at synoptic scales (horizontal wavelengths greater than several hundreds of kilometres), whereas a slope of $k^{-5/3}$ is found in the mesoscale regime. In between, a transition zone exists that extends over a wavelength range of about one order of magnitude. While spectral transform models using Eulerian time-stepping are in principle able to resolve the energy spectrum accurately down to their nominal spectral truncation wavelength (with the caveat that in practice some explicit filtering is needed in order to avoid a pile up of energy at the two-delta scale), grid-point models, and in general models using a semi-implicit semi-Lagrangian formulation, tend to under-represent the energy density at the shortest resolvable wavelengths (e.g. Skamarock, 2011). Defining the effective resolution as the wavelength at which the slope of the energy spectrum starts to deviate noticeably from the observed value (or a reference result obtained with higher model resolution), grid-point models using a C-grid discretization and horizontally explicit time-stepping usually have an effective resolution between $6\Delta x$ and $10\Delta x$ (Skamarock, 2011).

Kinetic energy spectra for the ICON non-hydrostatic dynamical core are displayed in Figure 7 for model grids ranging from R2B04 (160 km) to R2B07 (20 km). To avoid long spin-up times, the

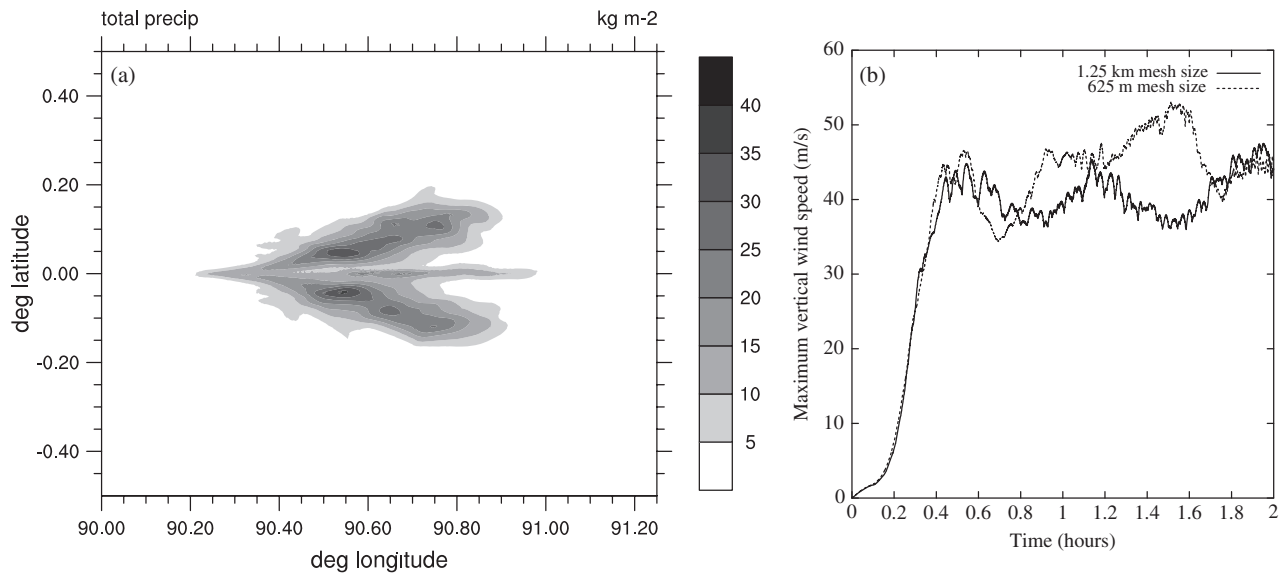


Figure 6. Results of the Weisman–Klemp supercell test (see text for details) after 2 h of simulation: (a) accumulated surface precipitation (kg m^{-2}) of the experiment with 625 m mesh size and (b) time series of maximum vertical velocity (m s^{-1}) for both experiments (see shading key). The ambient flow comes from the left.

simulations use a real-case set-up with full physics coupling, starting from interpolated operational IFS analysis data for 0000 UTC, 1 January 2011. In the vertical, 90 levels are used, with a model top at 75 km, and the total integration time is 20 days in each case. The scaling factors controlling diffusion were set to $f_d = 1/(500\Delta t)$ and $f_s = 0.0075$, respectively. To compute the spectra, vorticity and divergence, the latter, using a second-order accurate discretization (see section A1), were first interpolated vertically to pressure levels and then from the model grid to a regular latitude–longitude grid using RBFs. Each graph represents an average over 124 fields, based on 12 hourly output starting from day 5 for pressure levels of 300, 350, 400 and 450 hPa. It can be seen that the spectra for R2B04 to R2B06 start to deviate from those for the finer resolution(s) at wave numbers of about 35, 65 and 125, respectively, which corresponds to about $8\Delta x$ in each case. This lies well within the above-mentioned typical range for grid-point models with a C-grid discretization. In the corresponding results presented by Wan *et al.* (2013) for the hydrostatic dynamical core, the energy spectrum for R2B04 already starts to drop off at a wave number of 25, reflecting the larger amount of computational diffusion used in this core. Moreover, the graphs for R2B06 and R2B07 indicate a beginning transition from the synoptic-scale k^{-3} slope towards the $k^{-5/3}$ slope of the inertial subrange, although it is clear that a mesh size of 20 km is not yet sufficient to capture the transition fully. The largest curvature is found at about $6\Delta x$ in all four graphs, implying that even shorter waves are strongly under-represented on the model grids.

3.6. Preliminary results for NWP skill scores

For an operational NWP model, the predictive skill achieved in regular forecasting mode with data assimilation cycling is obviously the most important quality measure. Optimizing this skill is still in progress at the time of submission of this work. We therefore restrict ourselves to showing selected results for an off-line test suite with interpolated IFS analysis data, which have already reached a higher degree of consolidation. Experience shows that forecasting skills usually depend much more sensitively on the physics parametrizations and their mutual interaction than on the details of the dynamical core, but they can be used as an indication that the physics–dynamics coupling is implemented in an appropriate way. Moreover, real-case test suites are indispensable for assessing the numerical stability of a dynamical core, complementing the linear stability analysis provided in Appendix B.

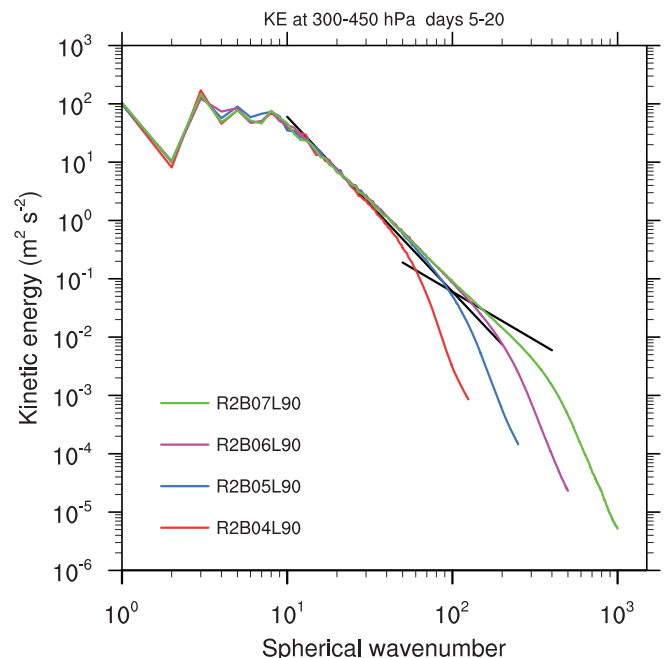


Figure 7. Kinetic energy spectra for a 20 day forecast in January initialized with operational IFS analysis data. Results are shown for different horizontal resolutions ranging from R2B04 (160 km) to R2B07 (20 km), using 90 vertical levels in each case. The two solid black lines indicates the expected slopes for the k^{-3} and $k^{-5/3}$ regimes.

The results presented in the following have been obtained for a horizontal mesh size of 40 km (R2B06) and 90 model levels with a top at 75 km, using the physics package described in section 2.7. For each day of January and June 2012, a seven-day forecast was conducted based on interpolated 0000 UTC operational IFS analysis data. The verification is performed against IFS analysis data at standard pressure levels on a 1.5° latitude–longitude grid, following the World Meteorological Organization (WMO) rules for analysis verification. For reference, an analogous test suite has been conducted with the operational hydrostatic GME, using the same horizontal mesh size and the operational 60 level set-up with a top at 5 hPa. Selected scores are displayed in Figure 8 for sea-level pressure and 500 hPa geopotential for the Northern Hemisphere.

It can be seen that both the anomaly correlations and the root-mean-square (RMS) errors are generally better for ICON than for GME in the two months considered here, indicating

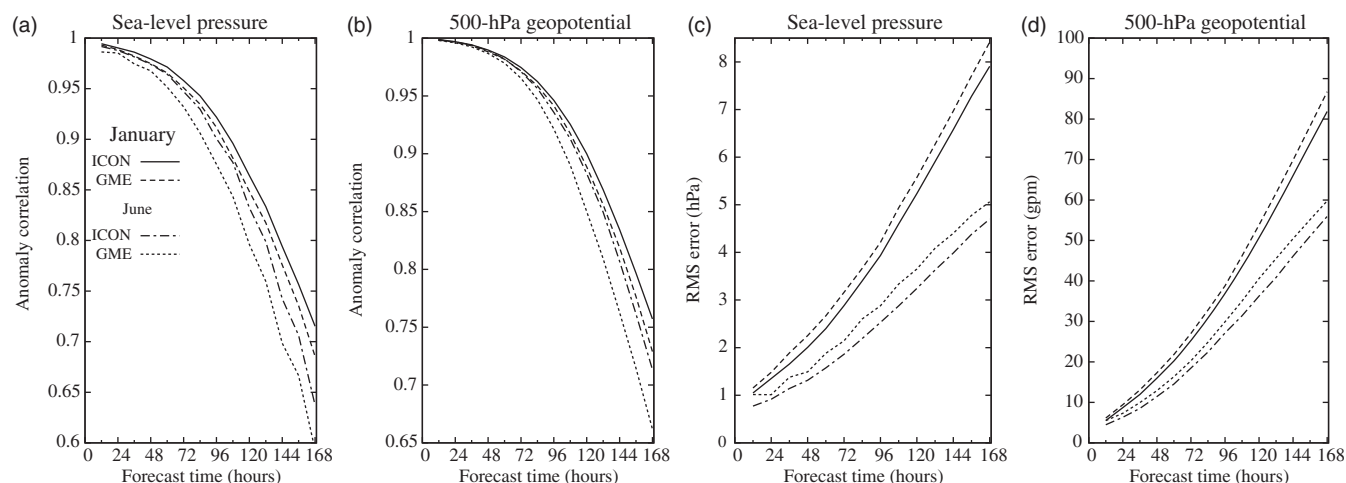


Figure 8. WMO standard skill scores against operational IFS analyses for the Northern Hemisphere (latitude $> 20^{\circ}\text{N}$), comparing ICON and GME with 40 km mesh size.

that ICON predicts the synoptic-scale evolution more accurately. The relative reduction of the RMS errors with respect to GME is typically about 10% in summer and a bit less in winter. Even larger improvements are found in the Tropics (not shown), which is primarily related to the fact that the biases (which dominate the geopotential RMS errors in the Tropics) are smaller in ICON, as a consequence of smaller temperature biases. Sensitivity tests have indicated that the more advanced turbulence, radiation and convection parametrizations contribute to the improved forecast quality of ICON, but we also noticed a substantial dependence on the tuning of the subgrid-scale orography scheme and on the interaction between the cloud-cover parametrization (which is still under development) and the radiation scheme.

In this context, it should be mentioned that, in contrast to pressure-based coordinate systems with a nominal model top at $p = 0$, which are typical for hydrostatic models, mass conservation does not imply conservation of the globally averaged surface pressure in a height-based coordinate system with a finite model top (such as used in ICON), because the mass lying *above* the model top may vary. With low model tops, this may give rise to unwanted pressure drifts (Klemp *et al.*, 2007). For our NWP configuration with its top at 75 km, however, two-month forecast experiments showed only a diurnal cycle with an amplitude of a few Pa but no indication of a trend. This remains unchanged when replacing Eq. (31) with Eq. (7) for the calculation of θ_v , supporting our hypothesis made above that the resulting conservation errors would be too small to become evident in real-case applications.

These results can be put in relation to the computational efficiency of ICON, which is significantly better than that of the operational hydrostatic GME, despite the fact that a non-hydrostatic dynamical core usually tends to be more expensive than a hydrostatic one. A large fraction of the improvement comes from the more efficient time-stepping scheme of ICON, which on the one hand allows for a larger time step for tracer advection and the physics parametrizations and on the other hand requires much less MPI communication (four halo exchange calls per dynamics time step) than the iterative elliptic solver of the semi-implicit Leapfrog time-stepping scheme used in GME. The latter results in a better scalability of ICON, so that run-time ratios between GME and ICON depend on the actual model configuration and the computational platform. As a practically relevant measure, we therefore take the amount of computational resources required to complete a seven-day forecast with the operational GME configuration (60 levels, 20 km mesh size) within the available time frame of 1 h. The corresponding time steps are 66 s for GME and 36/180 s for ICON when using a time-step ratio of 5 between the dynamical core and transport/physics. On the NEC SX-9 computer operational at DWD at the time of writing this article, ICON requires about one quarter of the resources of GME under these conditions.

4. Summary and conclusions

This article focuses on describing the non-hydrostatic dynamical core developed in the frame of the ICON project, in which DWD and MPI-M collaborate in order to establish a unified framework for a next-generation global NWP and climate modelling system. In addition, the strategy for physics–dynamics coupling is outlined and results for a hierarchy of tests with increasing complexity are presented.

The dynamical core is based on the set of prognostic variables suggested by Gassmann and Herzog (2008), using flux-form equations for the thermodynamic scalars ρ and θ_v . This allows local mass conservation to be achieved in a straightforward way. In the horizontal momentum equation, the nonlinear advection term is transformed into a vector-invariant form using the two-dimensional Lamb transformation. Time-stepping is performed with a two-time-level predictor–corrector scheme that is fully explicit, except for the terms describing vertical sound-wave propagation. However, to reduce the computational costs, only terms that are critical to accuracy or numerical stability are really evaluated twice per time step. Initial considerations to implement time splitting between acoustic terms and advection/gravity-wave terms within the dynamical core have been discarded, because it has been recognized that, in a global model extending up to the stratopause or beyond, the ratio between sound speed and the maximum wind speed tends to be too small for such an approach to be beneficial. Time splitting, with a typical time-step ratio of 4 or 5, is applied instead between the dynamical core on the one hand and tracer advection, the fast-physics parametrizations and horizontal diffusion on the other hand. Mass-consistent tracer transport is obtained by passing temporally averaged mass fluxes to the transport scheme. Compared with the hydrostatic dynamical core developed as an intermediate step by Wan *et al.* (2013), several refinements of the model numerics have been implemented in order to reduce the amount of computational diffusion required for numerical stability. Most importantly, the velocity components entering into the divergence operator are averaged such as to obtain (nearly) second-order accuracy and upwind-biased discretizations are used for the advection of the thermodynamic scalars. Besides imposing some implicit damping on small-scale structures, the latter reduce the numerical dispersion errors compared with second-order centred differences.

The results of the validation tests presented in section 3 confirm that the non-hydrostatic dynamical core of ICON performs well compared with reference solutions and better than the hydrostatic one in several important aspects, e.g. the grid imprinting measured by the steady-state Jablonowski–Williamson test, the phase-speed errors at coarse resolutions revealed by the corresponding baroclinic-wave test and the effective resolution according to kinetic energy spectra. While the phase-speed errors are still lower

in spectral transform models and some models with a pure finite-volume discretization, the kinetic energy spectra are within the typical range for grid-point models with a C-grid discretization. On the other hand, thanks to the z-level horizontal pressure-gradient discretization developed by Zängl (2012), the ICON model is able to cope with much steeper slopes than comparable models with terrain-following coordinates. Preliminary NWP test suites with interpolated IFS analysis data indicate that the forecast skill of ICON is already somewhat better than its predecessor GME, even though it has to be noted that work on optimizing and tuning the physics package of ICON is still in progress at the time of writing this article. At the same time, the computational efficiency of ICON is superior to that of GME by a factor of up to 4, depending on the model configuration and the degree of parallelization.

Thus, it can be concluded that the main development goals formulated in the initial phase of the ICON project have been fulfilled. We have achieved mass conservation, mass-consistent tracer transport and a substantial improvement of the computational efficiency compared with GME that exceeds the initial expectations. ICON also fulfils the basic preconditions for good scaling on future massively parallel computing platforms. Due to its compact discretization stencils and the efficient code-level organization of the computations, it needs a comparatively small amount of halo communication and, thanks to its horizontally explicit time-stepping scheme, it does not require global communication except for I/O and (optional) global diagnostics. Nevertheless, some aspects of the software infrastructure require further improvements, particularly with respect to memory scaling and I/O parallelization, before global applications at truly non-hydrostatic mesh sizes become feasible. Work on these issues is ongoing and we are confident we will be able to present related results in the near future.

Appendix A: Second-order accurate divergence on a triangular C grid

One of the main obstacles encountered during the ICON development is the fact that the basic divergence operator is only first-order accurate (Wan *et al.*, 2013). As discussed in detail by Gassmann (2011), this induces a rapidly oscillating, checkerboard-like pattern in the divergence field that causes numerical stability problems and tends to hide physically relevant structures. To overcome this problem, one can apply either a bilinear averaging of the locally computed divergence with that of the three neighbour cells or an appropriate averaging of the velocity components entering into the divergence computation. The first option was used as an intermediate step during the development process, but then abandoned, because it compromises local mass conservation and tracer-mass continuity. However, calculating the velocity averaging coefficients was found to work best on irregular spherical grids when basing it on the above-mentioned bilinear cell-averaging coefficients. The ensuing two-step procedure is described below.

A1. Cell averaging

The cell-averaging operator, denoted by $\overline{(\cdot)}^{\text{c-av}}$ in the following, is based on a simple bilinear averaging between a given cell (index 1) and its three neighbours (indices 2–4; see Figure A1), based on the equations

$$\sum_{i=2}^4 w_i (x_i - x_1) = 0, \quad \sum_{i=2}^4 w_i (y_i - y_1) = 0, \quad (\text{A1})$$

$$\sum_{i=1}^4 w_i = 1, \quad w_1 = 0.5, \quad (\text{A2})$$

where w_i denote the weighting coefficients and (x, y) is an appropriately defined local Cartesian coordinate system. As

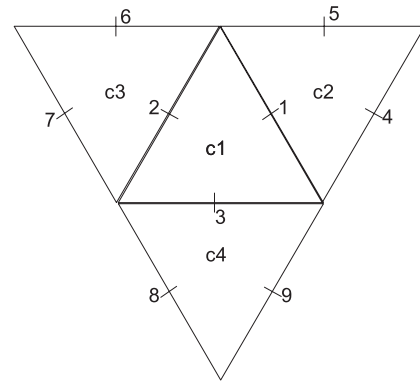


Figure A1. Four-point stencil for divergence and velocity averaging.

applying this operator to the divergence term in the continuity equation does not even provide global mass conservation, an appropriate modification of the weighting coefficients had been developed. It has been retained afterwards because the calculation of the velocity averaging coefficients described below turned out to benefit from it. The condition for global mass conservation is that the area-weighted contributions made by each cell sum up to exactly 1. For each cell,

$$w_c := w_1 + \frac{1}{a_1} \sum_{i=2}^4 \tilde{w}_i a_i = 1 \quad (\text{A3})$$

must be fulfilled, with a_i denoting cell areas and \tilde{w}_i the weighting coefficients by which cell 1 contributes to the averaging operator of each neighbour cell. As the equation system is now overspecified, an empirical iterative relaxation-diffusion approach had to be developed in order to find a reasonable compromise between the above requirements. Specifically, the local weight w_1 of each cell is allowed to deviate from 0.5 in order to fulfil Eq. (A3) under the side condition that the weights stay close to 0.5. The iterative procedure is as follows:

- compute residuals $r = w_c - 1$ on all cell points;
- modify the weights by $w_i = w_i - r c_i$, $i = 1 \dots 4$, using an empirically determined relaxation coefficient c_i of 0.46;
- compute a second set of residuals $R = \sum_{i=1}^4 w_i - 1$, followed by taking $w_i = w_i - \frac{1}{4} R$, $i = 1 \dots 4$, on all cell points; and
- limit w_1 such as to stay within $[0.5 - \epsilon, 0.5 + \epsilon]$, $\epsilon = 0.003$.

This iterative procedure is repeated 1000 times. In the last iteration, only $w_1 = w_1 - r$ is applied, in order to enforce global mass conservation exactly.

A2. Velocity averaging

Based on the weights of the bilinear cell averaging, another set of weighting coefficients is computed in order to obtain a nearly second-order accurate divergence operator without applying an *a posteriori* averaging to the divergence (which compromises local mass conservation and tracer mass consistency). Using the nomenclature of Figure A1, the averaged divergence operator

$$\overline{\tilde{\nabla} \cdot \mathbf{v}}^{\text{c-av}} = \sum_{i=1}^4 w_i \tilde{\nabla} \cdot \mathbf{v} \quad (\text{A4})$$

reads

$$\begin{aligned} \overline{\tilde{\nabla} \cdot \mathbf{v}}^{\text{c-av}} = & (g_{11}v_1 + g_{12}v_2 + g_{13}v_3) w_1 \\ & + (g_{21}v_1 + g_{24}v_4 + g_{25}v_5) w_2 \\ & + (g_{37}v_7 + g_{32}v_2 + g_{36}v_6) w_3 \\ & + (g_{48}v_8 + g_{49}v_9 + g_{43}v_3) w_4, \end{aligned} \quad (\text{A5})$$

where g_{ij} denote the geometric coefficients of the divergence operator (see Eq. (19)). We make the ansatz

$$\overline{\nabla \cdot \mathbf{v}}^{\text{c,av}} = g_{11}\overline{v_1}^{\text{c,av}} + g_{12}\overline{v_2}^{\text{c,av}} + g_{13}\overline{v_3}^{\text{c,av}}, \quad (\text{A6})$$

with

$$\overline{v_1}^{\text{c,av}} = a_{11}v_1 + a_{12}v_2 + a_{13}v_3 + a_{14}v_4 + a_{15}v_5, \quad (\text{A7})$$

$$\overline{v_2}^{\text{c,av}} = a_{21}v_1 + a_{22}v_2 + a_{23}v_3 + a_{26}v_6 + a_{27}v_7,$$

$$\overline{v_3}^{\text{c,av}} = a_{31}v_1 + a_{32}v_2 + a_{33}v_3 + a_{38}v_8 + a_{39}v_9,$$

which yields

$$\begin{aligned} \overline{\nabla \cdot \mathbf{v}}^{\text{c,av}} = & v_1(a_{11}g_{11} + a_{21}g_{12} + a_{31}g_{13}) \\ & + v_2(a_{12}g_{11} + a_{22}g_{12} + a_{23}g_{13}) \\ & + v_3(a_{13}g_{11} + a_{23}g_{12} + a_{33}g_{13}) \\ & + v_4a_{14}g_{11} + v_5a_{15}g_{11} + v_6a_{26}g_{12} \\ & + v_7a_{27}g_{12} + v_8a_{38}g_{13} + v_9a_{39}g_{13}. \end{aligned} \quad (\text{A8})$$

By comparison with Eq. (A5), the coefficients for v_4 to v_9 can be solved directly for a_{ij} . For example, for the target edge 1 one obtains $a_{14} = g_{24}w_2/g_{11}$ and $a_{15} = g_{25}w_2/g_{11}$ and the analogous equations for cell 2 (when redefined as central cell) provide the expressions for a_{12} and a_{13} . The local weight a_{11} turns out to be overdetermined, as one obtains

$$a_{11} = (g_{11}w_1 + g_{21}w_2 - a_{21}g_{12} - a_{31}g_{13})/g_{11} \quad (\text{A9})$$

and an analogous equation starting from cell 2. A compromise is found by weighting both equations with 0.5. Due to the above-mentioned conservation correction on the cell averaging weights, both equations give practically the same coefficient on spherical (icosahedral) grids, so that the loss of accuracy is very small. On planar grids with equilateral triangles, the coefficients are exactly identical for symmetry reasons. As a final step, the averaging coefficients are normalized in order to retain a constant wind field exactly. For edge 1, the condition reads exemplarily

$$a_{11} + \sum_{i=2}^5 a_{1i}\mathbf{e}_i \cdot \mathbf{e}_1 = 1, \quad (\text{A10})$$

where the \mathbf{e}_i denote the unit vectors of edge orientation. The ensuing normalization factors are usually within $[1 - 10^{-3}, 1 + 10^{-3}]$ if the conservation correction on the cell averaging weights has been applied before, but the normalization nevertheless exerts a measurably positive impact on the results of the steady-state Jablonowski–Williamson test (Figure 2).

Appendix B: Linear stability analysis

To inspect the stability properties of the predictor–corrector time integration scheme in combination with the spatial discretizations, a von Neumann stability analysis similar to that in Baldauf (2010) is performed. To this purpose, we consider a two-dimensional slice model, i.e. the discretization on the staggered, horizontally 2D triangular grid is replaced by a simplified one on a horizontally 1D staggered grid. Furthermore we neglect the Earth's curvature and do not consider metric terms of the terrain-following coordinate. Eqs (22)–(29) are linearized around a base state. This base state is defined by a constant base flow $u_0(\mathbf{r}, t) = U_0 = \text{constant}$, $w_0 = 0$ and, like the reference state introduced in section 2.4, the thermodynamic fields Θ_0 , ρ_0 and π_0 depend at most on z and fulfil the ideal gas law and the hydrostatic equation. In the following, the base state is characterized by two vertical inverse length scales: the heterogeneity $S_0 = \partial \log \rho_0 / \partial z$ and the stability parameter $B_0 = \partial \log \Theta_0 / \partial z$. The latter is related

to the Brunt–Väisälä frequency by $N^2 = gB_0$. Then, every field q is split into the base state and the first-order perturbation $q = q_0 + q'$ to end up with an equation system in the perturbation fields $\mathbf{q}' = (u', w', \rho', \pi')$. To this purpose, in particular the buoyancy term in Eq. (10) must be rewritten using the linearized ideal gas law:

$$-c_{\text{pd}}\Theta'_v \frac{\partial \pi_0}{\partial z} = g \frac{\Theta'_v}{\Theta_0} \approx -\frac{\rho'}{\rho_0} + \frac{c_v}{R} \frac{\pi'}{\pi_0}. \quad (\text{B1})$$

The von Neumann analysis assumes constant coefficients, in order to be able to perform a Fourier transform. This is approximately valid if we restrict the analysis to waves with vertical wavelengths λ_z that are much smaller than the vertical length-scales S_0^{-1} , B_0^{-1} and $(1/\pi_0 \cdot \partial \pi_0 / \partial z)^{-1}$. This holds for waves with $\lambda_z \ll 10$ km.

The linearized predictor–corrector scheme can be formulated as an ‘effective’ two-time-level scheme by

$$\begin{aligned} & \underbrace{\begin{pmatrix} -\mathbf{C}^{n+1} & -\mathbf{C}^{(n+1)*} & 0 \\ 0 & -\mathbf{P}^{(n+1)*} & 0 \\ 0 & 0 & 1 \end{pmatrix}}_{\mathbf{Q}^{(\text{im})}} \begin{pmatrix} \mathbf{q}'^{n+1} \\ \mathbf{q}'^{(n+1)*} \\ \mathbf{q}'^n \end{pmatrix} \\ & = \underbrace{\begin{pmatrix} \mathbf{C}^n & \mathbf{C}^{n*} & \mathbf{C}^{n-1} \\ \mathbf{P}^n & \mathbf{P}^{n*} & \mathbf{P}^{n-1} \\ 1 & 0 & 0 \end{pmatrix}}_{\mathbf{Q}^{(\text{ex})}} \begin{pmatrix} \mathbf{q}'^n \\ \mathbf{q}'^{n*} \\ \mathbf{q}'^{n-1} \end{pmatrix}, \end{aligned} \quad (\text{B2})$$

with the matrices for the predictor step

$$\mathbf{P}^{(n+1)*} = \begin{pmatrix} -1 & 0 & 0 & 0 \\ 0 & -1 & 0 & -\beta_1 S_2 \\ -S_3 & -\beta_1(S_4 + B_3) & -1 & 0 \\ -S_5 & -\beta_1(S_6 + B_4) & 0 & -1 \end{pmatrix}, \quad (\text{B3})$$

$$\mathbf{P}^n = \begin{pmatrix} 1 & 0 & 0 & -(1 + \alpha)S_1 \\ 0 & 1 & -B_1 & -\beta_2 S_2 + B_2 \\ 0 & -\beta_2(S_4 + B_3) & 1 - A_x^{(M)} & 0 \\ 0 & -\beta_2(S_6 + B_4) & 0 & 1 - A_x^{(M)} \end{pmatrix}, \quad (\text{B4})$$

$$\mathbf{P}^{n*} = \begin{pmatrix} -A_x & 0 & 0 & 0 \\ 0 & -A_x & 0 & 0 \\ 0 & 0 & 0 & 0 \\ 0 & 0 & 0 & 0 \end{pmatrix}, \quad (\text{B5})$$

$$\mathbf{P}^{n-1} = \begin{pmatrix} 0 & 0 & 0 & \alpha S_1 \\ 0 & 0 & 0 & 0 \\ 0 & 0 & 0 & 0 \\ 0 & 0 & 0 & 0 \end{pmatrix}, \quad (\text{B6})$$

and those for the corrector step

$$\mathbf{C}^{n+1} = \begin{pmatrix} -1 & 0 & 0 & 0 \\ 0 & -1 & 0 & -\beta_1 S_2 \\ -S_3 & -\beta_1(S_4 + B_3) & -1 & 0 \\ -S_5 & -\beta_1(S_6 + B_4) & 0 & -1 \end{pmatrix}, \quad (\text{B7})$$

$$\mathbf{C}^{(n+1)*} = \begin{pmatrix} -\gamma_1 A_x + D_u & D_w & 0 & 0 \\ 0 & -\gamma_1 A_x & -\delta_1 B_1 & \delta_2 B_2 \\ 0 & 0 & 0 & 0 \\ 0 & 0 & 0 & 0 \end{pmatrix}, \quad (\text{B8})$$

$$\mathbf{C}^n = \begin{pmatrix} 1 & 0 & 0 & -(1 + \alpha)S_1 \\ 0 & 1 & -\delta_2 B_1 & -\beta_2 S_2 + \delta_2 B_2 \\ 0 & -\beta_2(S_4 + B_3) & 1 - A_x^{(M)} & 0 \\ 0 & -\beta_2(S_6 + B_4) & 0 & 1 - A_x^{(M)} \end{pmatrix}, \quad (\text{B9})$$

$$\mathbf{C}^{n*} = \begin{pmatrix} -\gamma_2 A_x & 0 & 0 & 0 \\ 0 & -\gamma_2 A_x & 0 & 0 \\ 0 & 0 & 0 & 0 \\ 0 & 0 & 0 & 0 \end{pmatrix}, \quad (\text{B10})$$

$$\mathbf{C}^{n-1} = \begin{pmatrix} 0 & 0 & 0 & \alpha S_1 \\ 0 & 0 & 0 & 0 \\ 0 & 0 & 0 & 0 \\ 0 & 0 & 0 & 0 \end{pmatrix}. \quad (\text{B11})$$

The off-centring parameters are, as above, $\beta_2 = 1 - \beta_1$, $\gamma_2 = 1 - \gamma_1$ and $\delta_2 = 1 - \delta_1$.

The horizontal diffusion for the horizontal velocity can be described by a matrix \mathbf{Q}^{hd} , which is a 12×12 identity matrix with the exception of the element $Q_{1,1}^{\text{hd}} = 1 - K_4 \Delta t (\Delta x)^4 \delta_x \delta_x \delta_x \delta_x$.

The following operators have been used: for advection with second-order centred differences,

$$A_x = \Delta t U_0 \delta_x^{(2)}, \quad (\text{B12})$$

for the second-order Miura scheme,

$$A_x^{(M)} = \Delta t U_0 \delta_x^{(M)}, \quad (\text{B13})$$

for the sound processes in an Arakawa-C/Lorenz grid,

$$\begin{aligned} S_1 &= \Delta t c_p \Theta_0 \delta_x, & S_2 &= \Delta t c_p \Theta_0 \delta_z, \\ S_3 &= \Delta t \rho_0 \delta_x A_3, & S_4 &= \Delta t \rho_0 \delta_z, \\ S_5 &= \Delta t \frac{R}{c_v} \pi_0 \delta_x A_3, & S_6 &= \Delta t \frac{R}{c_v} \pi_0 \delta_z, \end{aligned} \quad (\text{B14})$$

for the buoyancy terms,

$$\begin{aligned} B_1 &= \Delta t \frac{g}{\rho_0} A_z, & B_2 &= \Delta t \frac{c_v}{R} \frac{g}{\pi_0} A_z, \\ B_3 &= \Delta t \frac{\partial \rho_0}{\partial z} A_z, & B_4 &= \Delta t \frac{R}{c_v} \pi_0 (S_0 + B_0) A_z, \end{aligned} \quad (\text{B15})$$

and for the divergence damping of fourth order,

$$D_u = -f_d \Delta t (\Delta x)^4 \delta_x \delta_x \delta_x \delta_x, \quad (\text{B16})$$

$$D_w = -f_d \Delta t (\Delta x)^4 \delta_x \delta_x \delta_x \delta_z. \quad (\text{B17})$$

The spatial operators and their Fourier representation are

$$\delta_x \phi_{j,k} = \frac{\phi_{j-\frac{1}{2},k} - \phi_{j+\frac{1}{2},k}}{\Delta x} \rightarrow i \frac{2 \sin \frac{k_x \Delta x}{2}}{\Delta x} \phi, \quad (\text{B18})$$

$$\delta_x^{(2)} \phi_{j,k} = \frac{\phi_{j-1,k} - \phi_{j+1,k}}{2 \Delta x} \rightarrow i \frac{\sin k_x \Delta x}{\Delta x} \phi, \quad (\text{B19})$$

$$\delta_z \phi_{j,k} = \frac{\phi_{j,k-\frac{1}{2}} - \phi_{j,k+\frac{1}{2}}}{\Delta z} \rightarrow i \frac{2 \sin \frac{k_z \Delta z}{2}}{\Delta z} \phi, \quad (\text{B20})$$

$$\begin{aligned} \delta_x^{(M)} &\rightarrow \frac{1 - e^{-ik_x \Delta x}}{\Delta x} \\ &\cdot \left(1 + \frac{1}{2} \left(1 - \frac{U_0 \Delta t}{\Delta x} \right) i \sin k_x \Delta x \right), \end{aligned} \quad (\text{B21})$$

$$A_z \phi_{j,k} = \frac{\phi_{j,k-\frac{1}{2}} + \phi_{j,k+\frac{1}{2}}}{2} \rightarrow \cos \frac{k_z \Delta z}{2} \phi, \quad (\text{B22})$$

$$\begin{aligned} A_3 \phi_{j,k} &= (1 - 2g_3) \phi_{j,k} + g_3 (\phi_{j-1,k} + \phi_{j+1,k}) \\ &\rightarrow [(1 - 2g_3) + 2g_3 \cos k_x \Delta x] \phi. \end{aligned} \quad (\text{B23})$$

A_3 with $g_3 = 0.2$ roughly mimics the effect of the five-point velocity averaging for the divergence operator in this simplified slice model.

Altogether, one has to determine the eigenvalues λ of the 12×12 matrix $\mathbf{Q}^{\text{hd}} \cdot (\mathbf{Q}^{(\text{im})})^{-1} \cdot \mathbf{Q}^{(\text{ex})}$. For a scheme that contains only centred spatial discretizations, this task can be considerably simplified. However, since the ICON dynamical core also contains upwind-biased schemes (Miura advection), one has to follow the methodology of Baldauf (2010), section 4: the 2D wave number space $(k_x \Delta x, k_z \Delta z) = [-\pi \dots \pi, -\pi \dots \pi]$ is sampled by 401×401 equidistant grid points and the maximum absolute eigenvalue is determined from the 12 eigenvalues in every point. Stability is assumed for $\max |\lambda| \leq 1$. Though this spectral radius is not a strong stability criterion, it is sufficient in most cases (see Skamarock and Klemp, 1992).

B1. Results

B1.1 Only sound terms

We consider only terms described by S_1, \dots, S_6 (Eq. (B14)); advection and buoyancy are switched off. Due to the vertically implicit scheme, the corrector step is already stable by itself and the predictor step has no significant influence on stability. A necessary condition for stability is $\alpha \geq 0$. The case $\alpha = 0$ corresponds to the standard horizontally explicit–vertically implicit (HE-VI) scheme. In this case, stability holds for all $\beta_1 \geq \frac{1}{2}$ and in the range $C_s \leq 1$, with the horizontal sound Courant number $C_s = c_s \Delta t / \Delta x$ and the sound velocity $c_s^2 = (c_p / c_v) R T_0$.

In the case $\alpha > 0$, the stability range for C_s decreases with increasing α : e.g. to $C_s \leq C_{s,\text{max}} \approx 0.84$ if $\alpha = 0.2$ and to $C_s \leq C_{s,\text{max}} \approx 0.70$ if $\alpha = 0.5$. Again, these ranges are valid for $\beta_1 \geq \frac{1}{2}$. In real-case model applications, however, the damping of horizontally propagating sound waves imposed by $\alpha > 0$ increases the usable time step.

B1.2 Only buoyancy terms

Now sound and advection terms are switched off. In the corrector step, the buoyancy terms (B_1, \dots, B_4 in Eq. (B15)) are described by a forward–backward scheme. Baldauf (2010) shows that such a discretization is stable for $N \cdot \Delta t \leq 2$. (For a system that uses p' and T' as prognostic variables, the acoustic cut-off frequency ω_a determines stability, whereas in the $p' - \pi'$ system considered here it is N .) However, this is only valid for $\beta_1 = 1$, i.e. if a ‘true’ backward step is used. For $\beta_1 < 1$, the combination of predictor and corrector steps is required for stability, i.e. a one-step Euler scheme would be unstable. In contrast to a ‘true’ forward–backward scheme, the stable range for $1/2 \leq \beta_1 \leq \beta_{1,\text{max}}$ decreases with increasing $N \cdot \Delta t$.

B1.3 Combination of sound, buoyancy and advection terms

Figure B1 shows the maximum amplification factor depending on k_x and k_z for an atmosphere at rest ($U_0 = 0$) and a stratification of $\partial T_0 / \partial z = -0.007 \text{ K m}^{-1}$. Two different strengths of the fourth-order horizontal diffusion on u , $K_4 \Delta t = 0.001$ and 0.01 , are considered, which damps very short, nearly horizontal waves. One can recognize that waves with a dimensionless wave number of roughly $K_z = k_z \Delta z < 0.1$ and thus $\lambda_z = 2\pi / k_z > 10 \text{ km}$ show a weak instability, whereas shorter waves are stable and nearly undamped, i.e. $|A|$ is close to 1. Here $\Delta x = 20 \text{ km}$, $\Delta z = 100 \text{ m}$ and a time step of $\Delta t = 45 \text{ s}$ were chosen, resulting in a sound

[†]In Baldauf (2010, Appendix A.a), the stability for the HE-VI scheme was limited to $1/2 \leq \beta_1 \leq 1$. However, one can easily see that $b^2 - a^2 c$ is non-positive for all β_1 (and $|S_x| \leq 1$). Therefore, stability holds for all $\beta_1 \geq 1/2$ and hence super-implicit weights are also usable.

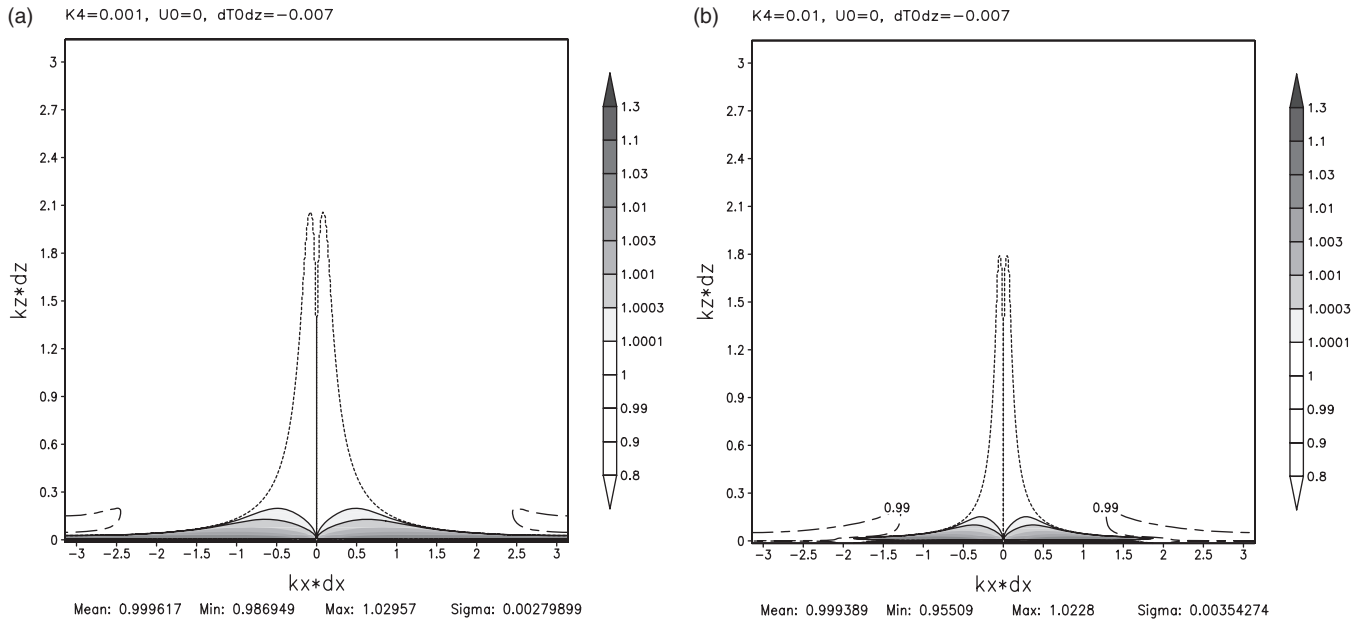


Figure B1. Amplification factor $|A|$ depending on horizontal and vertical (dimensionless) wave numbers $k_x \delta_x$ and $k_z \Delta z$ for sound and buoyancy terms (without advection) and different values for the horizontal diffusion $K_4 \Delta t$ of (a) 0.001 and (b) 0.01. $C_s = 0.7$, $dT_0/dz = -0.007 \text{ K m}^{-1}$ and $\beta_1 = 0.65$. Solid line: weak instability with $|A| = 1.0001$ and 1.0003 ; short-dashed: $|A| = 1$; and long-dashed: $|A| = 0.8, 0.9, 0.99$. For $K_z < 0$, use the symmetry $|A(-k_x, -k_z)| = |A(k_x, k_z)|$.

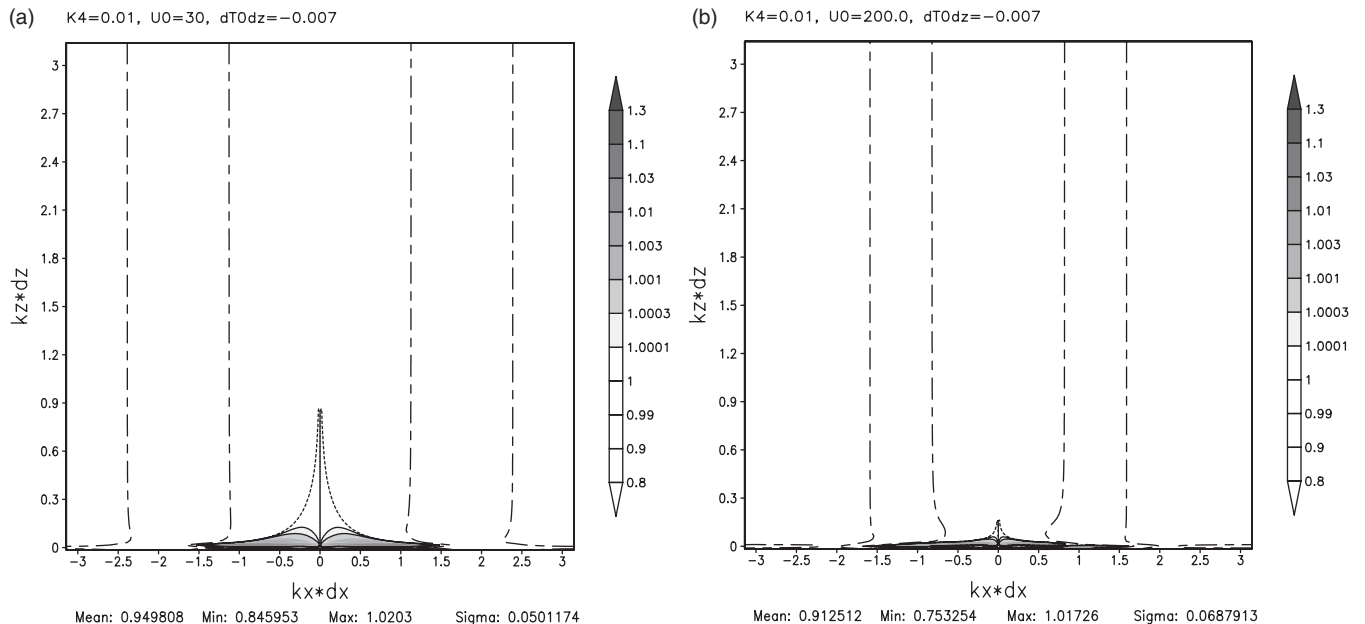


Figure B2. Analogous to Figure B1: now including advection with (a) $U_0 = 30 \text{ m s}^{-1}$ and (b) $U_0 = 200 \text{ m s}^{-1}$ and $K_4 \Delta t = 0.01$.

Courant number of $C_s = 0.7$. Other parameters are $\alpha = 0.5$, $\beta_1 = 0.65$, $\gamma_1 = 0.75$, $\delta_1 = 0.4$ and $f_d \Delta t = 0.001$.

In Figure B2, advection is added with base flow velocities of $U_0 = 30$ and 200 m s^{-1} , respectively. The slight damping inherent in both the Miura scheme and the centred-difference Matsuno scheme for $K_x \approx \pm\pi/2$ improves the stability even at high advection velocities. Thus, the stability range is extended to longer vertical wavelengths, whereas waves with very short horizontal wavelengths are now somewhat damped.

In summary, the only instability highlighted by our analysis pertains to waves with very long vertical wavelengths and a vertical propagation component. This needs to be interpreted with some care because, as discussed in the previous section, waves with a vertical wavelength above 10 km are formally outside the range of validity of our analysis. Moreover, the stabilizing effect of Rayleigh damping on w near the model top (see section 2.4) is not accounted for in the stability analysis. However, the instability diagnosed here seems to correspond with our experience that the off-centring parameter β_1 needs to be increased somewhat

beyond its default value when combining mesh sizes coarser than about 100 km (and thus relatively long time steps) with very high model tops (cf. section 2.4). For usual NWP applications, this is obviously not an issue, but it needs to be kept in mind for very coarsely resolved climate modelling applications.

Acknowledgements

The authors are indebted to all members of the ICON teams at DWD and MPI-M for their excellent work, without which the development of the ICON modelling system would not have been possible as a whole. Special thanks go to Almut Gassmann for her great preparatory work on the non-hydrostatic dynamical core, providing the basis for what has been reported here, and to Rainer Johanni and Leonidas Linardakis for their contributions to parallelizing and optimizing the ICON code. Moreover, we thank the two anonymous reviewers for their constructive comments, which led to a significant improvement of the manuscript.

References

- Baldauf M. 2010. Linear stability analysis of Runge–Kutta based partial time-splitting schemes for the Euler equations. *Mon. Weather Rev.* **138**: 4475–4496.
- Baldauf M, Reinert D, Zängl G. 2014. An analytical solution for linear gravity and sound waves on the sphere as a test for compressible, non-hydrostatic numerical models. *Q. J. R. Meteorol. Soc.*, doi: 10.1002/qj.2277.
- Bechtold P, Köhler M, Jung T, Doblas-Reyes F, Leutbecher M, Rodwell M, Vitart F, Balsamo G. 2008. Advances in simulating atmospheric variability with the ECMWF model: From synoptic to decadal time-scales. *Q. J. R. Meteorol. Soc.* **134**: 1337–1351.
- Bryan GH, Wyngaard JC, Fritsch JM. 2003. Resolution requirements for the simulation of deep moist convection. *Mon. Weather Rev.* **131**: 2394–2416.
- Doms G, Förstner J, Heise E, Herzog H-J, Mironov D, Raschendorfer M, Reinhardt T, Ritter B, Schrodin R, Schulz J-P, Vogel G. 2011. *A description of the Nonhydrostatic Regional COSMO Model, Part II: Physical parameterization*. Deutscher Wetterdienst: Offenbach, Germany. <http://www.cosmo-model.org> (accessed 9 May 2014).
- Gal-Chen T, Somerville R. 1975. Numerical solution of the Navier–Stokes equations with topography. *J. Comput. Phys.* **17**: 276–310.
- Gassmann A. 2011. Inspection of hexagonal and triangular C-grid discretizations of the shallow water equations. *J. Comput. Phys.* **230**: 2706–2721.
- Gassmann A. 2013. A global hexagonal C-grid non-hydrostatic dynamical core (ICON-IAP) designed for energetic consistency. *Q. J. R. Meteorol. Soc.* **139**: 152–175.
- Gassmann A, Herzog HJ. 2008. Towards a consistent numerical compressible non-hydrostatic model using generalized Hamiltonian tools. *Q. J. R. Meteorol. Soc.* **134**: 1597–1613.
- Heise E, Ritter B, Schrodin E. 2006. *‘Operational implementation of the multilayer soil model TERRA’*, Technical report. Deutscher Wetterdienst: Offenbach, Germany. <http://www.cosmo-model.org> (accessed 9 May 2014).
- Jablonski C, Williamson D. 2006a. A baroclinic instability test case for atmospheric model dynamical cores. *Q. J. R. Meteorol. Soc.* **132**: 2943–2975.
- Jablonski C, Williamson D. 2006b. *‘A baroclinic wave test case for dynamical cores of general circulation models: Model intercomparisons’*, Technical report. NCAR Technical Note NCAR/TN-469+STR. NCAR: Boulder, CO.
- Klemp JB, Skamarock WC. 2003. Numerical consistency of metric terms in terrain-following coordinates. *Mon. Weather Rev.* **131**: 1229–1239.
- Klemp JB, Skamarock WC, Dudhia J. 2007. Conservative split-explicit time integration methods for the compressible non-hydrostatic equations. *Mon. Weather Rev.* **135**: 2897–2913.
- Klemp JB, Dudhia J, Hassiotis AD. 2008. An upper gravity-wave absorbing layer for NWP applications. *Mon. Weather Rev.* **136**: 3987–4004.
- Lauritzen PH, Jablonowski C, Taylor M, Nair RD. 2010. Rotated versions of the Jablonowski steady-state and baroclinic wave test cases: A dynamical core intercomparison. *J. Adv. Model. Earth Syst.* **2**: 34 pp, doi: 10.3894/JAMES.2010.2.15.
- Lauritzen PH, Ullrich PA, Jablonowski C, Bosler PA, Calhoun D, Conley AJ, Enomoto T, Dong L, Dubey S, Guba O, Hansen AB, Kaas E, Kent J, Lamarque JF, Prather MJ, Reinert D, Shashkin VV, Skamarock WC, Sorensen B, Taylor MA, Tolstykh MA. 2014. A standard test case suite for two-dimensional linear transport on the sphere: Results from a collection of state-of-the-art schemes. *Geosci. Model Dev.* **7**: 105–145, doi: 10.5194/gmd-7-105-2014.
- Leuenberger D, Koller M, Fuhrer O, Schär C. 2010. A generalization of the SLEVE vertical coordinate. *Mon. Weather Rev.* **138**: 3683–3689.
- Lindborg E. 1999. Can the atmospheric kinetic energy spectrum be explained by two-dimensional turbulence? *J. Fluid Mech.* **388**: 259–288.
- Lott F, Miller M. 1997. A new subgrid-scale orographic drag parameterization: Its formulation and testing. *Q. J. R. Meteorol. Soc.* **123**: 101–127.
- Majewski D, Liermann D, Prohl P, Ritter B, Buchhold M, Hanisch T, Paul G, Wergen W, Baumgardner J. 2002. The operational icosahedral-hexagonal gridpoint model GME: Description and high-resolution tests. *Mon. Weather Rev.* **130**: 319–338.
- Mesinger F. 1977. Forward–backward scheme, and its use in a limited area model. *Beitr. Phys. Atmos.* **50**: 200–210.
- Miura H. 2007. An upwind-biased conservative advection scheme for spherical hexagonal-pentagonal grids. *Mon. Weather Rev.* **135**: 4038–4044.
- Mlawer EJ, Taubman SJ, Brown PD, Iacono MJ, Clough SA. 1997. Radiative transfer for inhomogeneous atmospheres: RRTM, a validated correlated-k model for the longwave. *J. Geophys. Res.* **102**: 16 663–16 682, doi: 10.1029/97JD00237.
- Narcovich F, Ward J. 1994. Generalized Hermite interpolation via matrix-valued conditionally positive definite functions. *Math. Comput.* **63**: 661–687.
- Nastrom GD, Gage KS. 1985. A climatology of atmospheric wavenumber spectra of wind and temperature observed by commercial aircraft. *J. Atmos. Sci.* **42**: 950–960.
- Orr A, Bechtold P, Scinocca J, Ern M, Janiskova M. 2010. Improved middle atmosphere climate and forecasts in the ECMWF model through a nonorographic gravity wave drag parameterization. *J. Clim.* **23**: 5905–5926.
- Quaddouri A, Lee V. 2011. The Canadian global environmental multiscale model on the Yin–Yang grid system. *Q. J. R. Meteorol. Soc.* **137**: 1913–1926.
- Raschendorfer M. 2001. The new turbulence parameterization of LM. *COSMO Newsl.* **1**: 89–97. <http://www.cosmo-model.org> (accessed 9 May 2014).
- Satoh M, Matsuno T, Tomita H, Miura H, Nasuno T, Iga S. 2008. Non-hydrostatic icosahedral atmospheric model (NICAM) for global cloud resolving simulations. *J. Comput. Phys.* **227**: 3486–3514.
- Schär C, Leuenberger D, Fuhrer O, Lüthi D, Girard C. 2002. A new terrain-following vertical coordinate formulation for atmospheric prediction models. *Mon. Weather Rev.* **130**: 2459–2480.
- Seifert A. 2008. A revised cloud microphysical parameterization for COSMO–LME. *COSMO Newsl.* **8**: 25–28. <http://www.cosmo-model.org> (accessed 9 May 2014).
- Skamarock W. 2011. Kinetic energy spectra and model filters. In *Numerical Techniques for Global Atmospheric Models* (1st edn). Springer: Berlin.
- Skamarock WC, Gassmann A. 2011. Conservative transport schemes for spherical geodesic grids: High-order flux operators for ODE-based time integration. *Mon. Weather Rev.* **139**: 2962–2975.
- Skamarock WC, Klemp JB. 1992. The stability of time-split numerical methods for the hydrostatic and the non-hydrostatic elastic equations. *Mon. Weather Rev.* **120**: 2109–2127.
- Skamarock WC, Klemp JB, Duda MG, Fowler LD, Park SH, Ringler TD. 2012. A multiscale non-hydrostatic atmospheric model using Centroidal Voronoi Tessellations and C-grid staggering. *Mon. Weather Rev.* **140**: 3090–3105.
- Smith RB. 1989. Hydrostatic airflow over mountains. *Adv. Geophys.* **31**: 59–81.
- Stevens B, Giorgetta M, Esch M, Mauritsen T, Crueger T, Rast S, Salzmann M, Schmidt H, Bader J, Block K, Brokopf R, Fast I, Kinne S, Kornbluh L, Lohmann U, Pincus R, Reichler T, Roeckner E. 2013. Atmospheric component of the MPI-M Earth System model: ECHAM6. *J. Adv. Model. Earth Syst.* **5**: 146–172, doi: 10.1002/jame.20015.
- Tomita H, Satoh M. 2004. A new dynamical framework of non-hydrostatic global model using the icosahedral grid. *Fluid Dyn. Res.* **34**: 357–400.
- Tomita H, Tsugawa M, Sato M, Goto K. 2001. Shallow water model on a modified icosahedral grid by using spring dynamics. *J. Comput. Phys.* **174**: 579–613.
- Ullrich PA, Jablonowski C. 2012. MCore: A non-hydrostatic atmospheric dynamical core utilizing high-order finite-volume methods. *J. Comput. Phys.* **231**: 5078–5108.
- Walko RL, Avissar R. 2008. The Ocean–Land–Atmosphere Model (OLAM). Part II: Formulation and tests of the non-hydrostatic dynamical core. *Mon. Weather Rev.* **136**: 4045–4062.
- Wan H. 2009. *‘Developing and testing a hydrostatic atmospheric dynamical core on triangular grids’*, PhD thesis, Reports on Earth System Science 65. Max Planck Institute for Meteorology: Hamburg, Germany.
- Wan H, Giorgetta MA, Zängl G, Restelli M, Majewski D, Bonaventura L, Fröhlich K, Reinert D, Rípodas P, Kornbluh L, Förstner J. 2013. The ICON-1.2 hydrostatic atmospheric dynamical core on triangular grids –Part 1: Formulation and performance of the baseline version. *Geosci. Model Dev.* **6**: 735–763.
- Weisman ML, Klemp JB. 1982. The dependence of numerically simulated convective storms on vertical wind shear and buoyancy. *Mon. Weather Rev.* **110**: 504–520.
- Weisman ML, Rotunno R. 2000. The use of vertical wind shear versus helicity in interpreting supercell dynamics. *J. Atmos. Sci.* **57**: 1452–1472.
- Zängl G. 2002. An improved method for computing horizontal diffusion in a sigma-coordinate model and its application to simulations over mountainous topography. *Mon. Weather Rev.* **130**: 1423–1432.
- Zängl G. 2012. Extending the numerical stability limit of terrain-following coordinate models over steep slopes. *Mon. Weather Rev.* **140**: 3722–3733.